

Correlations of Methyl Formate (CH₃OCHO), Dimethyl Ether (CH₃OCH₃) and Ketene (H₂CCO) in High-mass Star-forming Regions

Chuanshou Li,^{1*} Sheng-Li Qin,¹ Tie Liu,² Sheng-Yuan Liu,³ Mengyao Tang,⁴ Hong-Li Liu,¹ Li Chen,¹ Xiaohu Li,⁵ Fengwei Xu,^{6,7} Tianwei Zhang,^{8,9} Meizhu Liu,¹ Hongqiong Shi,¹ and Yuefang Wu⁷

¹*School of Physics and Astronomy, Yunnan University, Kunming 650091, People's Republic of China*

²*Shanghai Astronomical Observatory, Chinese Academy of Sciences, 80 Nandan Road, Shanghai 200030, People's Republic of China*

³*Academia Sinica Institute of Astronomy and Astrophysics, 11F AS/NTU Astronomy-Mathematics Building, No. 1, Section 4, Roosevelt Road, Taipei 10617, Taiwan*

⁴*Institute of Astrophysics, School of Physics and Electronic Science, Chuxiong Normal University, Chuxiong 675000, People's Republic of China*

⁵*Xinjiang Astronomical Observatory, Chinese Academy of Sciences, Urumqi 831399, China*

⁶*Kavli Institute for Astronomy and Astrophysics, Peking University, Beijing, 100871, People's Republic of China*

⁷*Department of Astronomy, School of Physics, Peking University, Beijing, 100871, People's Republic of China*

⁸*I. Physikalisches Institut, Universität zu Köln, Zùlpicher Straße 77, 50937 Köln, Germany*

⁹*Research Center for Intelligent Computing Platforms, Zhejiang Laboratory, Hangzhou 311100, P.R.China*

Accepted XXX. Received YYY; in original form ZZZ

ABSTRACT

We present high-spatial-resolution (0.7 to 1.0 arcsec) submillimeter observations of continuum and molecular lines of CH₃OCHO, CH₃OCH₃, and H₂CCO toward 11 high-mass star-forming regions using the Atacama Large Millimetre/submillimetre Array (ALMA). A total of 19 separate cores from 9 high-mass star-forming regions are found to be line-rich, including high-, intermediate-, and low-mass line-rich cores. The three molecules are detected in these line-rich cores. We map the emission of CH₃OCHO, CH₃OCH₃, and H₂CCO in 9 high-mass star-forming regions. The spatial distribution of the three molecules is very similar and concentrated in the areas of intense continuum emission. We also calculate the rotation temperatures, column densities, and abundances of CH₃OCHO, CH₃OCH₃, and H₂CCO under the local thermodynamic equilibrium (LTE) assumption. The abundances relative to H₂ and CH₃OH, and line widths of the three molecules are significantly correlated. The abundances relative to H₂, temperatures and line widths of the three molecules tend to be higher in cores with higher mass and outflows detected. The possible chemical links of the three molecules are discussed.

Key words: Astrochemistry – ISM: molecules – star: formation

1 INTRODUCTION

The astrochemical networks of many species have gradually been revealed. These species range from simple neutral molecules, molecular radicals, and ions to complex organic molecules (COMs). COMs are defined as C-bearing molecules with at least six atoms (Herbst & van Dishoeck 2009). At present, two major pathways for producing organic molecules have been proposed: (i) grain-surface chemical reactions (Hasegawa et al. 1992; Ruffle & Herbst 2000; Garrod et al. 2008; Ruaud et al. 2015); (ii) gas-phase chemical reactions (Duley & Williams 1984; Vasyunin & Herbst 2013; Balucani et al. 2015). Comparing the abundance and spatial distribution correlations of different species is an important mean to test chemical models and determine their formation paths. For example, interferometric observations showed a difference in the spatial distribution of O- and N-bearing molecules (Friedel & Snyder 2008; Csengeri et al. 2019; Qin et al. 2015, 2022), with N-bearing molecules tracing higher temperature gas than O-bearing molecules (Qin et al. 2010; Crockett et al. 2015; van 't Hoff et al. 2020). In particular, methyl formate (CH₃OCHO) and dimethyl ether (CH₃OCH₃) were found to have a

potential similarity (Jaber et al. 2014; Coletta et al. 2020; Peng et al. 2022; Chen et al. 2023). Nevertheless, the spatial similarity between CH₃OCHO and CH₃OCH₃ has not been systematically confirmed by interferometric observations with large samples.

Ketene (H₂CCO) has been proposed as an important precursor for the formation of COMs, such as acetic acid (CH₃COOH), acetamide (CH₃CONH₂), pyruvonitrile (CH₃COCN) and methyl acetate (CH₃COOCH₃) (Hudson & Loeffler 2013). However, there are still many uncertainties about how this molecule is produced (Charnley & Rodgers 2005; Ruiterkamp et al. 2007; Vasyunin & Herbst 2013; Maity et al. 2014; Krasnokutski et al. 2017; Fedoseev et al. 2022). CH₃OCHO, CH₃OCH₃, and H₂CCO are commonly detected in the same sources of hot molecular cores (HMCs) (Nummelin et al. 2000; Belloche et al. 2013), hot corinos (Bergner et al. 2017; Jørgensen et al. 2018; Bergner et al. 2019; Agúndez et al. 2019) or cold regions (Bacmann et al. 2012; Cernicharo et al. 2012; Jaber et al. 2014). Previous models have also shown that there may be chemical associations among the three molecules (Garrod & Herbst 2006; Garrod et al. 2008; Balucani et al. 2015; Charnley et al. 2001; Charnley & Rodgers 2005). Whereas the relationship of H₂CCO with the other two molecules has been barely explored from the observational side.

In this work, the correlations among CH₃OCHO, CH₃OCH₃, and

* E-mail: lichuanshou2021@163.com

H₂CCO are investigated toward 11 high-mass star-forming regions using Atacama Large Millimeter/submillimeter Array (ALMA) data. These data were observed as a pilot project for the ALMA Three-millimetre Observations of Massive Star-forming regions (ATOMS) survey (Liu et al. 2020). These 11 targets have large masses and luminosity (Xu et al. 2024), and show infall motion traced by the “blue profiles” observed by the HCN (4-3) lines (Liu et al. 2016). The paper is organized as follows. The observations and data reduction are described in Section 2. The observational results including continuum, line identifications, parameter calculation, and molecular emission maps are given in Section 3. We discuss the correlations of the three molecules and their implications for chemistry in Section 4. The main results and conclusions are summarized in Section 5.

2 OBSERVATIONS

The basic observational parameters and data reduction are described in Chen et al. (2024). Observations of 11 high-mass star-forming regions were performed from 18 to 20 May 2018 under the ALMA Cycle 5 project at Band 7 (ID: 2017.1.00545.S, PI: Tie Liu). A total of 43 antennas with a diameter of 12m were employed for observations (C43-1 configuration). The Band 7 observations offer 4 spectral windows (SPWs) centering at the frequency of 343.2 (SPW 31), 345.1 (SPW 29), 345.4 (SPW 25), and 356.7 GHz (SPW 27), respectively. Both SPWs 25 and 27 have a bandwidth of 469 MHz and a spectral resolution of 0.24 km s⁻¹, and are used to observe HCN (4-3) and HCO⁺ (4-3) lines, respectively. In this paper, we present the spectral line data of SPW 29 and SPW 31, both having a bandwidth of 1.88 GHz with a velocity resolution of 0.98 km s⁻¹. We used the TCLEAN task in Common Astronomy Software Applications (CASA; McMullin et al. 2007) to generate images of continuum and spectral cubes. Before the imaging processes, the bandpass, amplitude, and phase calibration were performed by running “ScriptForPI.py” offered by the ALMA team. For I14498, the phase calibrator is J1524-5903, and the flux and bandpass calibrator is J1427-4206. For I17220, the phase calibrator is J1733-3722, and the flux and bandpass calibrator is J1924-2914. As for the other 7 sources, the phase calibrator is J1650-5044, and the flux and bandpass calibrators are J1924-2914, J1427-4206, and J1517-2422. The continuum image was constructed from all line-free channels of four spectral windows. Self-calibrations were performed to improve the qualities of continuum images. Totally 3 rounds of phase self-calibrations and 1 round of amplitude self-calibration had been conducted to all continuum data of 11 sources. During the self-calibration, we used the “hogbom” deconvolution algorithm with a weighting parameter of “briggs”. The robust parameter of “briggs” weighting can be set from -2.0 to 2.0 to smoothly customize trade-offs between resolution and imaging sensitivity. The “robust=0.5” was set to balance the sensitivity and resolution of our images. Following self-calibration, the Root-Mean-Square (rms) noise of the source I15520 was reduced by approximately 19%, the source I14498, I16351 and I17220 by about 3%, and the source I15596, I16060, I16076, I16272 and I17204 were barely improved. The primary beam correction had also been performed. Finally, the solutions from the self-calibration of continuum images were applied to line cubes. The synthesized beam sizes of continuum images and line cubes range from 0.7 to 1.0 arcsec. The average sensitivity is better than 8.0 mJy beam⁻¹ per channel for line cubes, and better than 2.5 mJy beam⁻¹ for continuum images.

3 RESULTS

3.1 Continuum Emission

We perform multi-component two-dimensional Gaussian fits to 870 μ m continuum emission using the CASA-*imfit* function. A total of 145 dense cores were resolved in 11 high-mass star-forming regions (Chen et al. 2024). We have checked the spectra towards the 145 cores one by one, and found that 19 separate cores in 9 regions have multiple line emissions of CH₃OCHO or CH₃OCH₃ or H₂CCO. From Figure 1 and A1, these 19 cores show rich line emission. The ALMA 870 μ m continuum emission from 9 high-mass star-forming regions is shown in Figure 2. The positions of 19 line-rich cores are labeled. For the other two of the 11 high-mass star-forming regions (IRAS 14382-6017 and IRAS 17204-3636), the line transitions of the three molecules were not detected. The absence of HMCs from these two sources was affirmative by cross-matching with the ALMA Band 3 dataset (Qin et al. 2022).

For the estimation of the core masses and the molecular hydrogen column densities, the commonly used method assumes that the dust emission is optically thin and in local thermodynamic equilibrium (LTE). Under these assumptions, the core masses and source-averaged H₂ column densities can be estimated by the expressions (Kauffmann et al. 2008):

$$M_{\text{core}} = \frac{S_{\nu}\eta D^2}{\kappa_{\nu}B_{\nu}(T)}, \quad (1)$$

$$N(\text{H}_2) = \frac{S_{\nu}\eta}{\mu m_{\text{H}}\Omega\kappa_{\nu}B_{\nu}(T)}, \quad (2)$$

where S_{ν} is integrated flux density, $\eta = 100$ is gas-to-dust mass ratio (Lis et al. 1991; Hasegawa et al. 1992), D is the distance to the core (Liu et al. 2020) and the uncertainty takes 10% (Baug et al. 2020; Liu et al. 2022) when calculating the uncertainty of the core mass, κ_{ν} is the dust mass absorption coefficient, $B_{\nu}(T)$ is the Planck function at dust temperature T , $\mu = 2.8$ is the mean molecular weight of the gas (Kauffmann et al. 2008), m_{H} is the mass of the hydrogen atom, and Ω is the solid angle corresponding to the deconvolved size of the core. In our case, $\kappa_{870\mu\text{m}}$ takes a value of 1.89 cm² g⁻¹, which is interpolated from the table given in Ossenkopf & Henning (1994), assuming grains with thin ice mantles and a gas density of 10⁶ cm⁻³. The dust temperatures of dense cores are assumed to be the rotation temperatures of CH₃OCHO, which is considered to be dust temperature probe (Favre et al. 2011). The parameters of 19 line-rich cores are listed in Table 1. In Table 1, we also list whether these cores are associated with outflows. The presence of outflows is identified by searching for red-blue lobes around continuum sources using the CO (3-2), HCN (4-3), and SiO (2-1) lines (Baug et al. 2020).

The source-averaged optical depths of the continuum can be calculated by the following formula (Frau et al. 2010; Gieser et al. 2021):

$$\tau_{\nu} = -\ln\left(1 - \frac{S_{\nu}}{\Omega B_{\nu}(T)}\right). \quad (3)$$

The derived $\tau_{870\mu\text{m}}$ ranges from 6.2 $\times 10^{-3}$ to 1.4 $\times 10^{-1}$ for the 19 dense cores, so the optically thin assumption is reasonable. I15520, I16060, I16071, I16076, I16351, and I17220 were found to be associated with the ultra-compact (UC) HII regions traced by the H40 α lines (Qin et al. 2022; Liu et al. 2022). Free-free emissions from UC HII regions in the submillimeter band are weak, which have less contribution to the continuum flux.

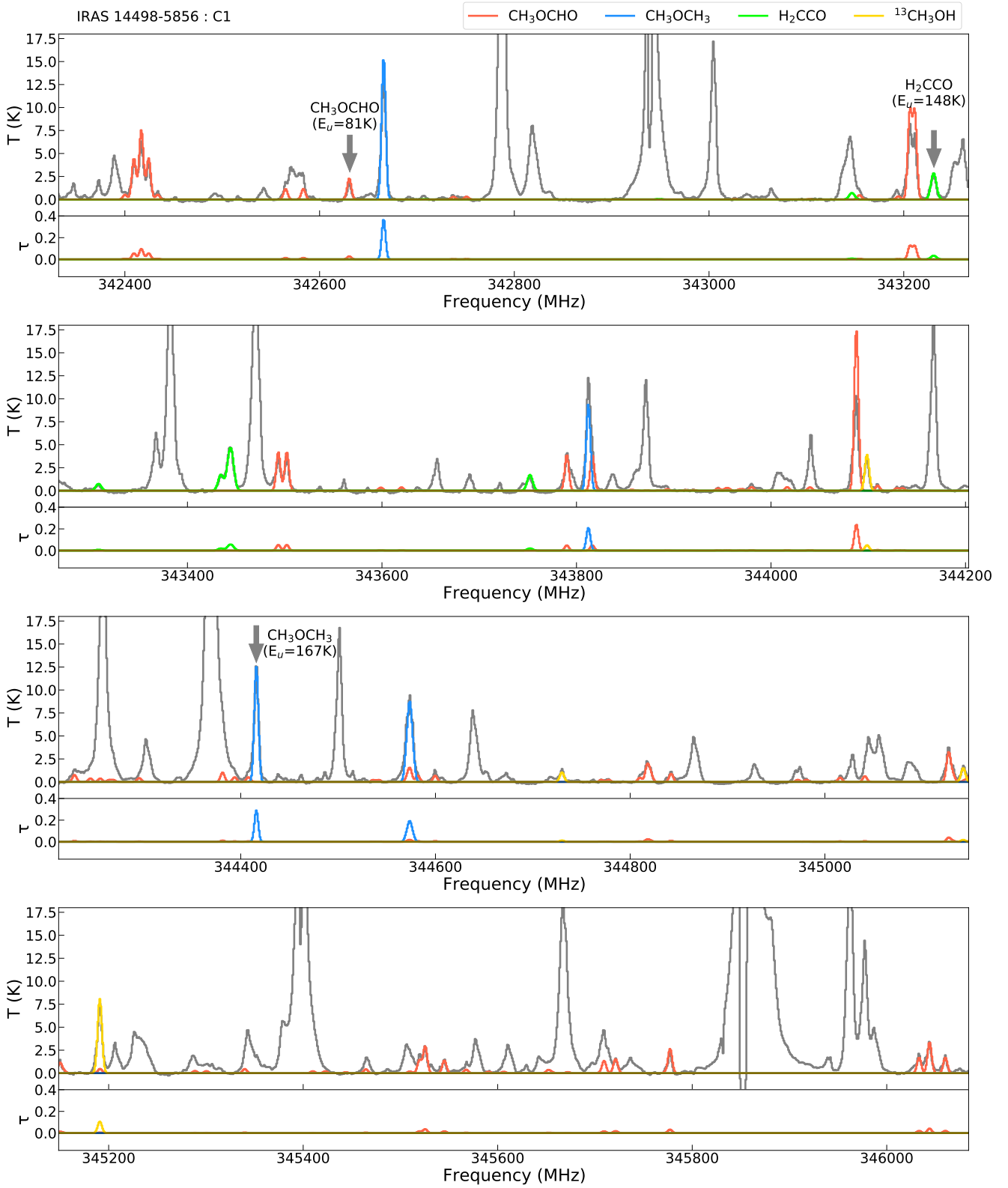


Figure 1. Sample spectra and optical depths of the three molecules for I14498 C1. The observed spectra are shown in gray curves and the XCLASS modeled spectra are shown in color curves. The small panel below each spectrum shows the optical depths of the XCLASS modeled spectra. The gray arrows represent the transitions used as integrated intensity maps in Figure 2. The spectra and optical depths of other line-rich cores are shown in Figure A1.

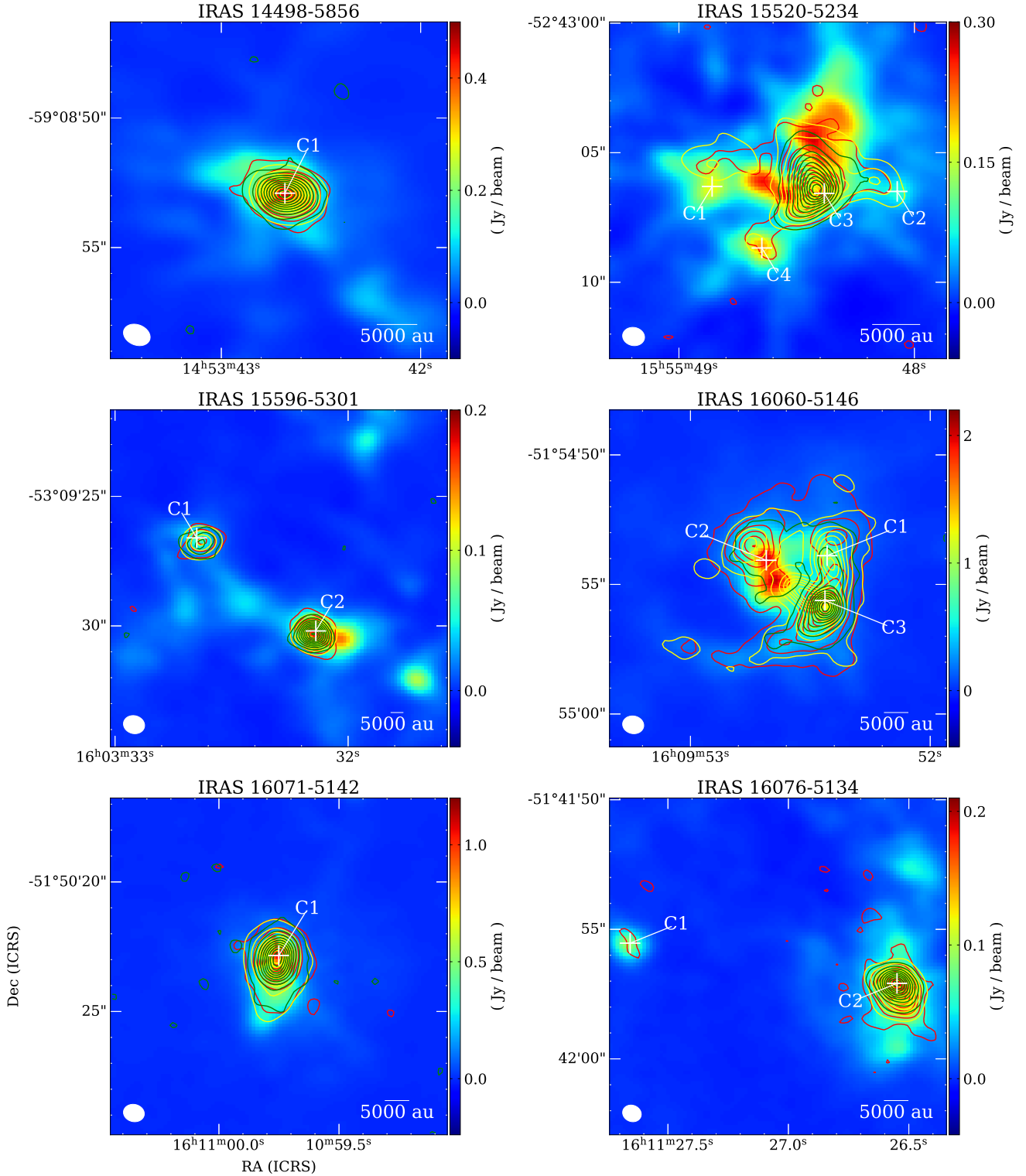
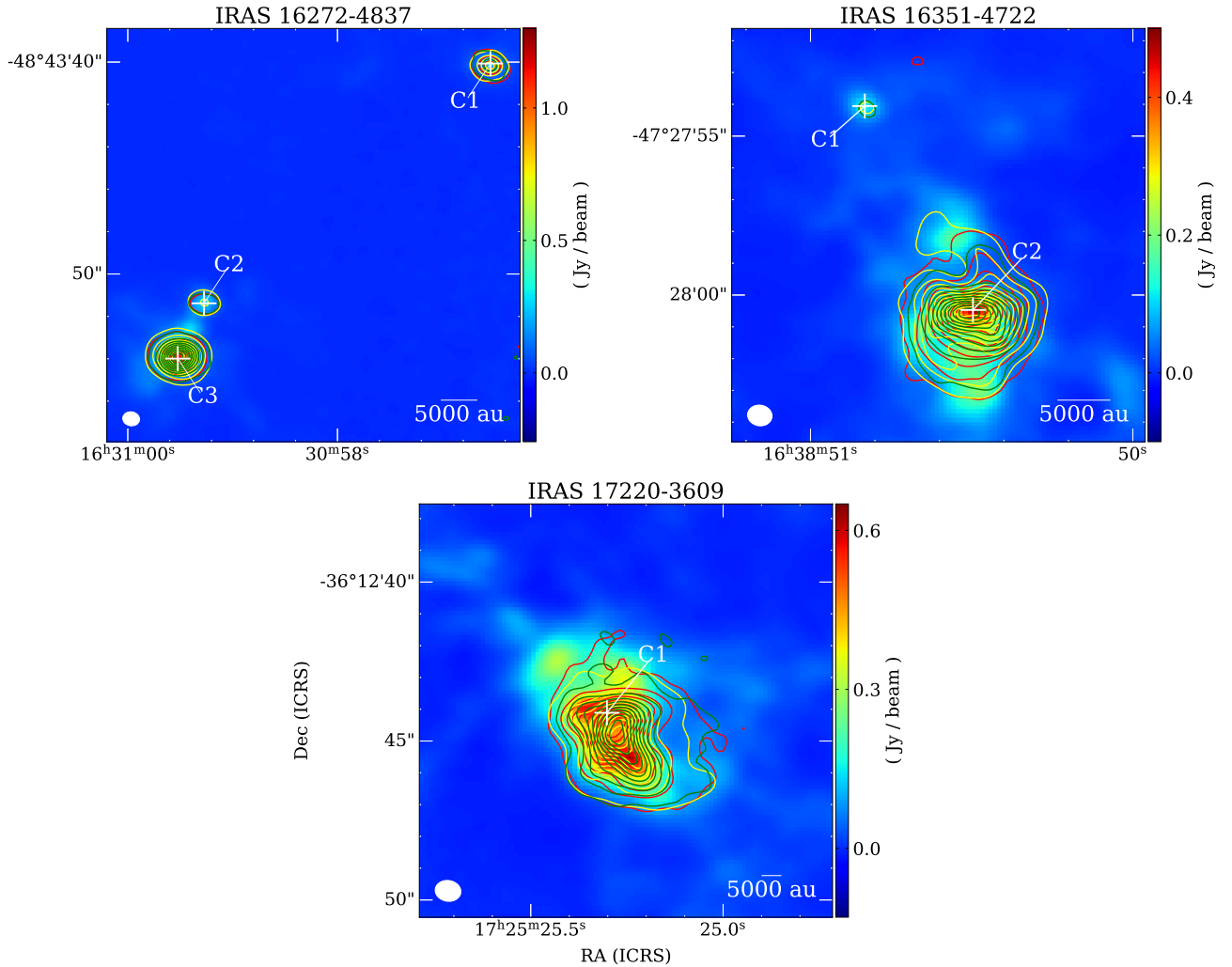


Figure 2. Continuum emission at $870\ \mu\text{m}$ overlaid with integrated intensities of CH_3OCHO , CH_3OCH_3 , and H_2CCO in 9 high-mass star-forming regions. The dense cores are labeled by declination (Dec) order. The green, yellow, and red contours represent CH_3OCHO at 342572 MHz ($E_u = 81\ \text{K}$), CH_3OCH_3 at 344358 MHz ($E_u = 167\ \text{K}$), and H_2CCO at 343173 MHz ($E_u = 148\ \text{K}$), respectively. The contour levels are stepped by 10% of the peak values, with the outermost contour levels as follows: I14498: 5%, I15520: 3%, I15596: 8%, I16060: 2%, I16071: 2%, I16076: 6%, I16272: 2%, I16351: 2%, I17220: 2% of the peak values. The synthesized beam sizes are shown on the lower left, the scalebars are shown on the lower right, and the continuum emission colorbars are shown on the right.

Figure 2. – *continued*

3.2 Line Identifications

We extracted the spectra from the continuum peak positions of these dense cores. Then the spectral line transitions are identified using the eXtended CASA Line Analysis Software Suite (XCLASS¹; Möller et al. 2017). XCLASS searches for molecular line parameters in the Jet Propulsion Laboratory (JPL²; Pickett et al. 1998) and the Cologne Database for Molecular Spectroscopy (CDMS³; Müller et al. 2001, 2005). The value of the partition functions in the XCLASS have 110 different temperature intervals between 1.072 and 1000 K. Assuming that the molecular gas satisfies the LTE condition, the XCLASS solves the radiative transfer equation and produces synthetic spectra for specific molecular transitions by taking into account beam dilution, dust attenuation, line opacity, and line blending. In the XCLASS modeling, the input parameters are the size (θ), rotational temperature (T), column density (N), line width (ΔV), and velocity offset (V_{off}) of each molecule. In our study, we took the deconvolved

sizes (see Table 1) of the continuum sources as molecular component sizes. To better fit the rotation temperature, column density, and line width parameters, we further employed Modeling and Analysis Generic Interface for eXternal numerical codes (MAGIX; Möller et al. 2013). The MAGIX optimizes these molecular component parameters within the given range and provides the corresponding error estimates. The parameter ranges are set based on the initial guesses provided by XCLASS fitting. Note that in our case the optical depths of the continuum cores are less than 1.4×10^{-1} and then the dust attenuation effect can be ignored.

Transitions are considered as detection if the line intensities exceed 3σ noise level. CH₃OCHO, CH₃OCH₃, H₂CCO, and CH₃OH lines are detected in all 19 line-rich cores, and ¹³CH₃OH lines are detected in 16 line-rich cores. Figure 1 shows the sample spectra and optical depths of molecular transitions toward I14498 C1. The spectra and optical depths of molecular transitions toward the other 18 cores are presented in Figure A1 of Appendix A. The overall results of the detected spectral lines are summarized as follows:

¹ <https://xclass.astro.uni-koeln.de>

² <http://spec.jpl.nasa.gov>

³ <http://cdms.de>

Table 1. Physical Parameters of the Continuum Sources.

Region	Core	D (kpc)	R.A. (h : m : s)	DEC. (° : ′ : ″)	θ_{dec} maj(″) × min(″)	R_{core} (au)	I_{peak} (mJy beam ⁻¹)	S_{ν} (mJy)	T (K)	M_{core} (M_{\odot})	N (H ₂) (cm ⁻²)	Outflows	Mass Classification
I14498-5856	C1	3.2	14:53:42.7	-59:08:52.8	3.2×1.9	7890	340±22	2830±200	102±6	21.4±2.9	(2.1±0.2)e+23	1	H
I15520-5234	C1	2.7	15:55:48.9	-52:43:06.1	2.9×2.0	6502	149±11	1600±120	80±10	11.2±2	(1.6±0.2)e+23	0	H
	C2		15:55:48.1	-52:43:06.5	1.9×1.4	4404	80±3	440±18	70±36	3.6±1.9	(1.1±0.6)e+23	0	I
	C3		15:55:48.4	-52:43:06.5	2.0×1.4	4518	200±5	1128±35	102±4	6.1±0.7	(1.8±0.1)e+23	1	I
	C4		15:55:48.6	-52:43:08.5	3.1×1.9	6553	142±17	1510±190	105±37	7.9±3	(1.1±0.4)e+23	1	I
I15596-5301	C1	10.1	16:03:32.6	-53:09:26.6	1.3×0.8	10300	55±4	160±16	100±23	12.3±3.3	(7.0±1.8)e+22	1	H
	C2		16:03:32.1	-53:09:30.3	2.2×0.9	14212	166±9	799±54	110±39	55.4±20.7	(1.7±0.6)e+23	0	H
I16060-5146	C1	5.3	16:09:52.4	-51:54:53.8	2.2×1.2	8611	843±48	5000±330	112±7	93.6±12.7	(7.6±0.7)e+23	0	H
	C2		16:09:52.7	-51:54:53.9	1.6×1.1	7031	1530±160	6520±810	136±4	99.2±16.1	(1.2±0.2)e+24	1	H
	C3		16:09:52.4	-51:54:55.6	1.6×1.2	7344	1220±100	5500±550	110±2	105.0±15	(1.2±0.1)e+24	1	H
I16071-5142	C1	5.3	16:10:59.8	-51:50:23.1	1.8×1.0	7111	849±107	3840±580	127±10	62.9±12.4	(7.5±1.3)e+23	1	H
I16076-5134	C1	5.3	16:11:27.7	-51:41:55.6	0.9×0.7	4207	93±1	218±5	87±11	5.4±0.9	(1.8±0.2)e+23	1	I
	C2		16:11:26.5	-51:41:57.4	2.3×1.5	9844	160±11	1410±110	98±10	30.5±5	(1.9±0.2)e+23	1	H
I16272-4837	C1	2.9	16:30:57.3	-48:43:40.1	1.0×0.8	2594	212±8	549±27	106±3	3.3±0.4	(2.9±0.2)e+23	0	I
	C2		16:30:58.6	-48:43:51.4	1.2×0.6	2461	252±14	638±49	102±17	4.0±0.8	(3.9±0.7)e+23	0	I
	C3		16:30:58.8	-48:43:54.0	0.8×0.8	2320	1144±51	2560±160	115±4	14.0±1.7	(1.6±0.1)e+24	1	H
I16351-4722	C1	3.0	16:38:50.8	-47:27:54.1	0.8×0.6	2078	113±3	220±9	90±9	1.7±0.2	(2.3±0.3)e+23	0	L
	C2		16:38:50.5	-47:28:00.8	2.2×1.9	6134	320±45	3010±470	170±10	11.6±2.3	(1.9±0.3)e+23	1	H
I17220-3609	C1	8.0	17:25:25.3	-36:12:44.1	3.6×1.4	17960	554±19	5870±220	107±13	263.1±42.6	(4.9±0.6)e+23	0	H

Notes. The distances of the 9 high-mass star-forming regions are taken from [Liu et al. \(2020\)](#). The positions, deconvolved sizes, peak flux densities, and integrated flux densities of 19 dense cores are obtained from multi-component 2D Gaussian fitting of the 870 μm continuum with CASA. The radii are derived from the equation $R_{\text{core}} = \sqrt{\theta_{\text{maj}}\theta_{\text{min}}} / 3600 \times \pi / 180 \times D$. The core masses and molecular hydrogen column densities are calculated in Eq. (1) and Eq. (2) of Section 3.1. The mass classification is discussed in Section 4.1. Outflows, 0 = the outflows are not detected, 1 = the outflows are detected (taken from [Baug et al. 2020](#)).

Table 2. Physical Parameters of CH₃OCHO, CH₃OCH₃, H₂CCO, ¹³CH₃OH, and CH₃OH.

Region	Core	CH ₃ OCHO			CH ₃ OCH ₃			H ₂ CCO			¹³ CH ₃ OH	CH ₃ OH
		T (K)	N (cm ⁻²)	ΔV_{dec} (km s ⁻¹)	T (K)	N (cm ⁻²)	ΔV_{dec} (km s ⁻¹)	T (K)	N (cm ⁻²)	ΔV_{dec} (km s ⁻¹)	N (cm ⁻²)	N (cm ⁻²)
I14498-5856	C1	102±6	(2.8±0.7)e+16	4.1±0.1	65±4	(2.8±0.3)e+16	3.9±0.2	105±2	(2.5±0.3)e+15	5.5±0.6	(2.5±0.9)e+16	(1.1±0.4)e+18 ^a
I15520-5234	C1	80±10	(8.5±1.7)e+14	1.7±0.7	66±14	(8.0±1.4)e+15	2.7±0.2	85±39	(3.0±1.1)e+14	2.6±1.0	...	(1.4±0.3)e+16
	C2	70±36	(1.5±0.4)e+15	0.5±0.4	63±10	(1.1±0.2)e+16	1.6±0.1	110±23	(1.3±0.3)e+14	1.1±0.1	...	(9.5±1.3)e+16
	C3	102±4	(9.5±0.5)e+16	1.5±0.1	80±1	(4.8±0.8)e+16	1.1±0.2	105±8	(2.8±0.4)e+15	1.6±0.1	(9.5±0.7)e+16	(4.1±0.3)e+18 ^a
	C4	105±37	(7.5±3.8)e+14	1.1±0.6	77±38	(2.1±0.8)e+15	1.3±0.1	88±46	(1.3±0.7)e+14	1.4±0.6	...	(7.2±1.2)e+15
I15596-5301	C1	100±23	(1.7±0.7)e+16	4.7±0.6	58±8	(1.6±0.5)e+16	5.2±0.6	105±14	(1.0±0.5)e+15	5.4±0.9	(5.7±1.1)e+15	(2.2±0.4)e+17 ^a
	C2	110±39	(2.4±1.0)e+16	3.9±0.5	60±6	(2.6±0.1)e+16	4.9±0.6	127±19	(1.5±0.3)e+15	3.0±0.7	(1.6±0.4)e+16	(6.1±1.5)e+17 ^a
I16060-5146	C1	112±7	(3.8±0.8)e+16	2.4±0.3	65±2	(6.7±0.2)e+16	2.7±0.2	136±12	(2.0±0.5)e+15	3.3±0.3	(3.2±0.3)e+16	(1.1±0.1)e+18 ^a
	C2	136±4	(2.4±0.7)e+16	4.9±0.6	137±5	(9.2±1.0)e+15	6.2±0.6	173±1	(5.3±0.2)e+15	5.0±0.6	(3.7±0.9)e+16	(1.3±0.3)e+18 ^a
	C3	110±2	(1.4±0.1)e+17	4.9±0.7	80±13	(5.7±0.2)e+16	5.9±0.6	147±4	(9.0±0.4)e+15	4.7±0.7	(1.2±0.1)e+17	(4.2±0.4)e+18 ^a
I16071-5142	C1	127±10	(2.0±0.1)e+17	7.4±0.5	80±4	(1.8±0.1)e+17	6.2±0.7	138±6	(1.6±0.1)e+16	7.9±0.8	(3.6±0.3)e+17	(1.3±0.1)e+19 ^a
I16076-5134	C1	87±11	(3.6±0.3)e+15	2.6±0.8	58±10	(3.1±0.6)e+15	2.8±0.9	130±8	(2.0±0.2)e+14	3.4±0.9	(2.0±0.3)e+15	(7.0±0.1)e+16 ^a
	C2	98±10	(3.8±0.3)e+16	4.5±0.5	51±3	(5.8±0.4)e+16	6.4±0.6	135±9	(2.3±0.5)e+15	5.4±0.7	(3.6±0.6)e+16	(1.3±0.2)e+18 ^a
I16272-4837	C1	106±3	(1.0±0.1)e+17	4.4±0.5	79±2	(9.0±0.3)e+16	4.4±0.5	103±3	(1.0±0.1)e+16	4.9±0.5	(9.0±2.9)e+16	(3.7±1.2)e+18 ^a
	C2	102±17	(5.0±0.7)e+16	5.6±0.6	62±1	(3.4±0.8)e+16	4.9±0.5	135±10	(3.5±0.7)e+15	7.4±0.7	(7.2±0.7)e+16	(3.0±0.3)e+18 ^a
	C3	115±4	(7.0±0.9)e+17	2.8±0.5	109±5	(3.5±0.5)e+17	4.5±0.6	125±7	(4.8±0.7)e+16	3.7±0.7	(5.5±0.2)e+17	(2.3±0.1)e+19 ^a
I16351-4722	C1	90±9	(1.0±0.1)e+16	1.6±0.6	50±4	(7.2±0.1)e+15	1.6±0.7	123±19	(4.8±0.8)e+14	2.1±0.8	(7.0±0.5)e+15	(2.9±0.2)e+17 ^a
	C2	170±10	(2.0±0.1)e+17	5.3±0.6	93±5	(1.3±0.2)e+17	4.9±0.6	159±33	(1.3±0.5)e+16	5.9±0.8	(1.6±0.2)e+17	(6.6±0.8)e+18 ^a
I17220-3609	C1	107±13	(1.2±0.2)e+17	3.9±0.5	65±15	(1.5±0.1)e+17	5.9±0.5	102±10	(1.2±0.1)e+16	3.8±0.6	(6.5±1.1)e+16	(1.2±0.2)e+18 ^a

Notes. The rotation temperatures T and column densities N are model fitting results. The ΔV_{dec} is deconvolved line widths. ^a The column densities of CH₃OH in these cores are obtained from the column densities of ¹³CH₃OH using Eq. (7).

1. Most transitions in each core are optically thin ($\tau < 1$).
2. In each core, more than three lines are detected for CH₃OCHO, CH₃OCH₃, and H₂CCO, and CH₃OCHO presents more lines than CH₃OCH₃ and H₂CCO.
3. In all cores, the CH₃OCHO and CH₃OCH₃ have larger line intensities, while the line intensities of H₂CCO are generally smaller.

The rotational transitions of CH₃OCHO, CH₃OCH₃, and H₂CCO detected in 19 dense cores are listed in Table B1 of Appendix B. The upper level energy ranges of CH₃OCHO, CH₃OCH₃, and H₂CCO are 80 to 590 K, 73 to 167 K and 148 to 474 K, respectively. These three molecules, especially CH₃OCHO and H₂CCO, cover a wide range of upper level energies, which is conducive to the constraints of rotational temperatures and column densities.

3.3 Column Densities, Rotation Temperatures, Line Widths, and Molecular Abundances

The MAGIX optimization results for CH₃OCHO, CH₃OCH₃, and H₂CCO in 19 dense cores are shown in Table 2. The column densities mainly range from 10^{15} to 10^{17} cm⁻² for CH₃OCHO and CH₃OCH₃, and from 10^{14} to 10^{16} cm⁻² for H₂CCO. The upper level energies of H₂CCO lines are larger than 148 K (see Section 3.2), and the column densities of H₂CCO are lower, which can explain its weaker line intensities than the other two molecules. The rotation temperature ranges of CH₃OCHO, CH₃OCH₃, and H₂CCO are 70 to 170 K, 50 to 137 K and 85 to 173 K, respectively. The rotation temperatures of CH₃OCH₃ in most cores are generally lower than those of CH₃OCHO and H₂CCO, possibly because our 870 μ m observations of the CH₃OCH₃ lines have lower upper level energies (see Table B1) and then the hot components of the cores are not sampled. CH₃OCHO and H₂CCO should trace hotter components than CH₃OCH₃. Considering the overestimation of line widths due to velocity resolution of 0.98 km s⁻¹ (see Section 2), we adopt the deconvolved line widths by the following formula:

$$\Delta V_{\text{dec}} = \sqrt{\Delta V^2 - \Delta v^2}, \quad (4)$$

where ΔV is the fitted line width convolved with the velocity resolution Δv . We computed the molecular abundances relative to H₂ and CH₃OH by the following formula:

$$f_{\text{H}_2} = N/N(\text{H}_2), \quad (5)$$

$$f_{\text{CH}_3\text{OH}} = N/N(\text{CH}_3\text{OH}), \quad (6)$$

where N is the column density of the specific molecule, $N(\text{H}_2)$ is the column density of H₂ (see Table 1), and $N(\text{CH}_3\text{OH})$ is the column density of CH₃OH (see Table 2). Due to the blending of CH₃OH lines with other molecular lines in 16 line-rich cores, we then fit ¹³CH₃OH line transitions and derive the column densities of CH₃OH by the column densities of ¹³CH₃OH (see Table 2) multiplied by the ¹²C/¹³C ratios from the following formula (Yan et al. 2019):

$$^{12}\text{C}/^{13}\text{C} = (5.08 \pm 1.10)R_{\text{GC}} + (11.86 \pm 6.60), \quad (7)$$

where R_{GC} (in kpc) represents the distance from the Galactic Center (Liu et al. 2020). In the other 3 line-rich cores without ¹³CH₃OH detected, the column densities of CH₃OH are obtained through direct fitting, where the CH₃OH lines are not blended. The abundances of CH₃OCHO, CH₃OCH₃, and H₂CCO relative to H₂ and CH₃OH are listed in Table 3.

3.4 The Molecular Emission Maps

The integrated intensity maps of CH₃OCHO at 342572 MHz ($E_u = 81$ K), CH₃OCH₃ at 344358 MHz ($E_u = 167$ K), and H₂CCO at 343173 MHz ($E_u = 148$ K) in 9 high-mass star-forming regions are shown in Figure 2. The emission peaks of CH₃OCHO, CH₃OCH₃, and H₂CCO are consistent, and the spatial distribution of the three molecules is similar. These results suggest that there may be physical or chemical links among the three molecules. In addition, there is no difference in the spatial distributions of different energy level transitions of CH₃OCHO in the 9 high-mass star-forming regions, as shown in Figure C1 of Appendix C. From Figure 2 and Figure C1, the line emissions of CH₃OCHO, CH₃OCH₃, and H₂CCO are primarily distributed around intense continuum emission. I15520, I16060, and I17220 are found to be associated with intense UC HII regions, while I16071, I16076, and I16351 are associated with weaker UC HII regions (Qin et al. 2022; Zhang et al. 2023). In I15520, I16060, and I17220, the line emissions are offset from the continuum cores, and CH₃OCHO, CH₃OCH₃, and H₂CCO also show irregular emissions in these regions, likely due to the influence of UC HII regions.

4 DISCUSSION

4.1 Core Classification

Unlike HMCs, which are associated with the formation of massive stars, hot corinos are found around low-mass protostars. Typical hot corinos are small in size ($\lesssim 200$ AU) and show a rich chemistry (Cazaux et al. 2003; Bottinelli et al. 2004; Maret et al. 2004; Bottinelli et al. 2007). Intermediate-mass hot cores (IMHCs) provide the link between HMCs and hot corinos, although it has rarely been reported (Sánchez-Monge et al. 2010; Palau et al. 2011; Fuente et al. 2014). In high-mass star-forming regions, dense cores exist within massive reservoirs, and the mass of the stars formed is uncertain. Therefore, it is difficult to identify hot corinos and IMHCs (sometimes they are simply assumed to be HMCs) in high-mass star-forming regions.

In Table 1, we classify 19 line-rich cores into three groups according to their mass (further material accretion or loss may occur), namely 12 high-mass line-rich cores (H; $> 8 M_{\odot}$), 6 intermediate-mass line-rich cores (I; $2 - 8 M_{\odot}$), and 1 low-mass line-rich core (L; $< 2 M_{\odot}$). Moreover, the 11 high-mass star-forming regions are subsamples of Qin et al. (2022), who reported 60 HMCs from 146 high-mass star-forming regions at ALMA resolutions of $\sim 1.2 - 1.9$ arcsec. Our currently higher spatial resolution observations reveal that part of the HMCs detected in previous works actually host multiple line-rich cores with different masses. (see Qin et al. 2022 and our Figure 2).

4.2 Abundance, Temperature and Line Width Correlations

In Figure 3, we compare the CH₃OCHO, CH₃OCH₃, and H₂CCO abundances relative to H₂ in 19 dense cores. CH₃OCHO and CH₃OCH₃ show a strong abundance correlation (the Pearson correlation coefficient $r = 0.82$). The abundance correlation between CH₃OCH₃ and H₂CCO is significant ($r = 0.80$). CH₃OCHO and H₂CCO show the stronger abundance correlation ($r = 0.93$) than the other two pairs of molecules. Figure 4 shows the relationships of the abundances of the three molecules relative to CH₃OH in 19 dense cores. The abundances of CH₃OCHO and CH₃OCH₃ relative to CH₃OH mainly range from 10^{-2} to 10^{-1} , while the abundance of H₂CCO relative to CH₃OH mainly ranges from 10^{-3} to 10^{-2} .

Table 3. Molecular Abundances Relative to H₂ and CH₃OH.

Region	Core	CH ₃ OCHO		CH ₃ OCH ₃		H ₂ CCO	
		f _{H₂}	f _{CH₃OH}	f _{H₂}	f _{CH₃OH}	f _{H₂}	f _{CH₃OH}
I14498-5856	C1	(1.4±0.4)e−07	(2.5±1.1)e−02	(1.4±0.2)e−07	(2.5±1.0)e−02	(1.2±0.2)e−08	(2.3±0.9)e−03
I15520-5234	C1	(5.3±1.3)e−09	(6.1±1.8)e−02	(5.0±1.1)e−08	(5.7±1.6)e−01	(1.9±0.7)e−09	(2.1±0.9)e−02
	C2	(1.3±0.8)e−08	(1.6±0.5)e−02	(9.9±5.4)e−08	(1.2±0.3)e−01	(1.2±0.7)e−09	(1.4±0.4)e−03
	C3	(5.3±0.4)e−07	(2.3±0.2)e−02	(2.7±0.5)e−07	(1.2±0.2)e−02	(1.6±0.2)e−08	(6.9±1.1)e−04
	C4	(6.8±4.3)e−09	(1.0±0.6)e−01	(1.9±1.0)e−08	(2.9±1.2)e−01	(1.2±0.8)e−09	(1.8±1.0)e−02
I15596-5301	C1	(2.4±1.2)e−07	(7.8±3.5)e−02	(2.3±0.9)e−07	(7.4±2.7)e−02	(1.4±0.8)e−08	(4.6±2.5)e−03
	C2	(1.4±0.8)e−07	(3.9±1.9)e−02	(1.6±0.6)e−07	(4.3±1.1)e−02	(9.1±3.7)e−09	(2.5±0.8)e−03
I16060-5146	C1	(5.0±1.1)e−08	(3.4±0.8)e−02	(8.8±0.8)e−08	(6.0±0.6)e−02	(2.6±0.7)e−09	(1.8±0.5)e−03
	C2	(2.0±0.6)e−08	(1.9±0.7)e−02	(7.6±1.3)e−09	(7.1±1.8)e−03	(4.4±0.6)e−09	(4.1±1.0)e−03
	C3	(1.2±0.2)e−07	(3.3±0.4)e−02	(4.8±0.5)e−08	(1.4±0.1)e−02	(7.7±0.9)e−09	(2.1±0.2)e−03
I16071-5142	C1	(2.7±0.5)e−07	(1.5±0.1)e−02	(2.4±0.4)e−07	(1.4±0.1)e−02	(2.1±0.4)e−08	(1.2±0.1)e−03
I16076-5134	C1	(2.0±0.3)e−08	(5.1±1.0)e−02	(1.7±0.4)e−08	(4.4±1.1)e−02	(1.1±0.2)e−09	(2.9±0.6)e−03
	C2	(2.0±0.3)e−07	(2.9±0.5)e−02	(3.1±0.4)e−07	(4.5±0.8)e−02	(1.2±0.3)e−08	(1.8±0.5)e−03
I16272-4837	C1	(3.4±0.4)e−07	(2.7±0.9)e−02	(3.1±0.2)e−07	(2.4±0.8)e−02	(3.4±0.4)e−08	(2.7±0.9)e−03
	C2	(1.3±0.3)e−07	(1.7±0.3)e−02	(8.6±2.6)e−08	(1.1±0.3)e−02	(8.9±2.4)e−09	(1.2±0.3)e−03
	C3	(4.5±0.7)e−07	(3.1±0.4)e−02	(2.2±0.4)e−07	(1.6±0.2)e−02	(3.1±0.5)e−08	(2.1±0.3)e−03
I16351-4722	C1	(4.3±0.6)e−08	(3.5±0.4)e−02	(3.1±0.3)e−08	(2.5±0.2)e−02	(2.1±0.4)e−09	(1.7±0.3)e−03
	C2	(1.1±0.2)e−06	(3.0±0.4)e−02	(7.0±1.6)e−07	(2.0±0.4)e−02	(7.0±2.9)e−08	(2.0±0.8)e−03
I17220-3609	C1	(2.4±0.5)e−07	(1.0±0.2)e−01	(3.0±0.4)e−07	(1.3±0.2)e−01	(2.4±0.4)e−08	(1.0±0.2)e−02

Notes. The abundances of CH₃OCHO, CH₃OCH₃, and H₂CCO relative to H₂ and CH₃OH are calculated in Eq. (5) and Eq. (6) of Section 3.3.

The abundances of the three molecules relative to CH₃OH in our observations are consistent with those observed in high-mass star-forming regions (Bøgelund et al. 2019; Peng et al. 2022; Chen et al. 2023; López-Gallifa et al. 2024), intermediate-mass star-forming regions (Palau et al. 2011; Fuente et al. 2014; Ospina-Zamudio et al. 2018), low-mass star-forming regions (Taquet et al. 2015; Lefloch et al. 2017; Jørgensen et al. 2018), Galactic center molecular clouds (Requena-Torres et al. 2006, 2008), and comets (Biver & Bockelée-Morvan 2019). The correlation coefficients of the abundances relative to CH₃OH are 0.69 between CH₃OCHO and CH₃OCH₃, 0.75 between CH₃OCH₃ and H₂CCO, and 0.79 between CH₃OCHO and H₂CCO, indicating positive correlations. The obvious abundance correlation relative to CH₃OH between CH₃OCHO and CH₃OCH₃ was also observed in four different interstellar sources, including 1 HMC, 1 hot corino, and 2 comets (López-Gallifa et al. 2024). From Figure 3 and Figure 4, the relative abundances of CH₃OCHO to CH₃OCH₃ are almost constant equal to 1. Chen et al. (2023) also found a constant relative abundance of ~ 1 between CH₃OCHO and CH₃OCH₃ toward 19 protostars with different luminosities. This ratio is consistent with the observations from low-, intermediate- and high-mass star-forming regions (Jaber et al. 2014; Rivilla et al. 2017; Ospina-Zamudio et al. 2018; Coletta et al. 2020; Peng et al. 2022). In Figure 3 and Figure 4, we also compared our results with the molecular abundances relative to H₂ and CH₃OH in other HMCs and hot corinos. The abundance correlations relative to H₂ and CH₃OH in these sources agree with the results in our observations but more dispersed than our samples, which is most likely due to different spatial resolution and spectral setup of these observations. These results suggest that the formation of the three molecules may be closely related, i.e., they may have similar production conditions, or even share a common chemical reaction network.

In Figure 5, we compare the rotation temperatures of the three

molecules. The temperature correlation coefficient of CH₃OCHO and CH₃OCH₃ is 0.62, CH₃OCH₃ and H₂CCO is 0.47, and CH₃OCHO and H₂CCO is 0.64. The results indicate that the rotation temperatures have no significant correlations among the three molecules. The results observed by Coletta et al. (2020) toward 13 high-mass star-forming regions also showed a poor temperature correlation ($r = 0.45$) between CH₃OCHO and CH₃OCH₃, but the overall temperature ranges of the two molecules are similar. In fact, most of the temperatures of the three molecules in our case are in the range of tens of Kelvin, which is probably the reason why there is no apparent trend in temperature.

The line width relationships of the three molecules are shown in Figure 6. The CH₃OCHO and H₂CCO show strong line width correlation ($r = 0.95$), followed by CH₃OCHO and CH₃OCH₃ ($r = 0.88$), and by CH₃OCH₃ and H₂CCO ($r = 0.79$). This agrees with the line width correlation of CH₃OCHO and CH₃OCH₃ observed in 13 high-mass star-forming regions (Coletta et al. 2020). This implies that the three molecules may trace the similar kinematics.⁴

In Figures 3, 5, and 6, the H cores are shifted to the upper right relative to the I and L cores, indicating a tendency for the abundances relative to H₂, temperatures and line widths of the three molecules to be higher in massive line-rich cores. In Figure 7, we also compare molecular abundances relative to H₂ and CH₃OH, rotation temperatures and line widths of the cores with and without detected outflows (see Table 1). The abundances relative to H₂, temperatures and line

⁴ In our case, the line widths of the three molecules are almost entirely contributed by non-thermal motions: $\Delta V_{\text{dec}} \sim \Delta V_{\text{NT}} = \sqrt{\Delta V_{\text{dec}}^2 - 8 \ln 2 \frac{kT_{\text{ex}}}{m}}$, where ΔV_{NT} is the line width contributed by non-thermal motions, k is the Boltzmann constant, T_{ex} is the excitation temperature of the molecule, and m is the molecular mass.

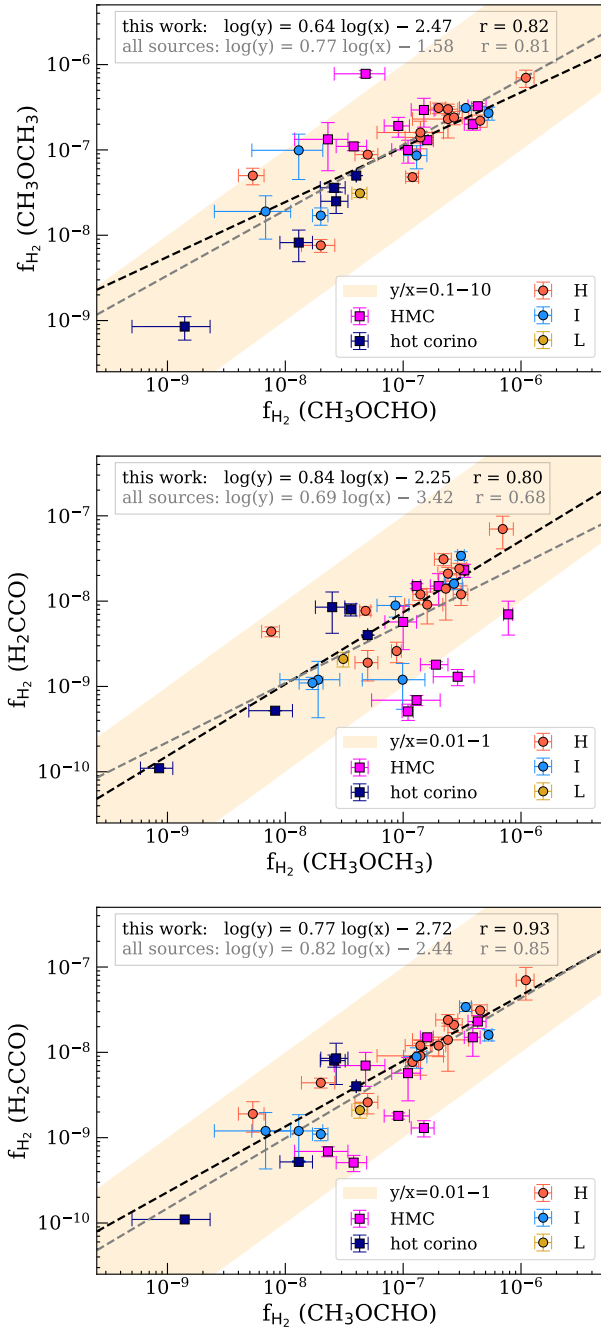


Figure 3. Comparison among the molecular abundances of CH₃OCHO, CH₃OCH₃, and H₂CCO relative to H₂. The colored circles represent the different types of cores in this work (H = high-mass line-rich core, I = intermediate-mass line-rich core, and L = low-mass line-rich core), while the colored squares represent the sources in the literature (References: HMCs: Feng et al. 2015; Bøgelund et al. 2019; Peng et al. 2022; hot corinos: Taquet et al. 2015; Lefloch et al. 2017; Ospina-Zamudio et al. 2018; Bianchi et al. 2019). The orange areas indicate the relative abundance ranges of molecules. The black dashed lines and the gray dashed lines are linear least-squares fits of this work and all sources, respectively. The fitting results and Pearson correlation coefficients (r) are shown on the top left.

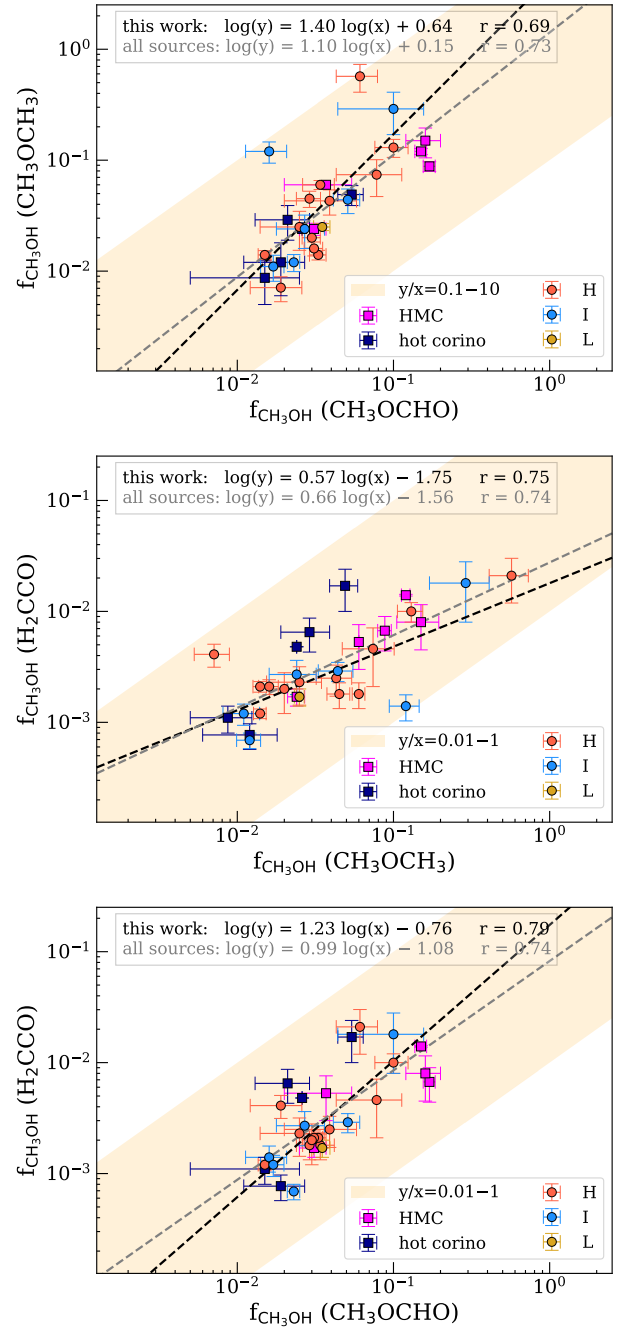


Figure 4. Comparison among the molecular abundances of CH₃OCHO, CH₃OCH₃, and H₂CCO relative to CH₃OH. The colored circles represent the different types of cores in this work (H = high-mass line-rich core, I = intermediate-mass line-rich core, and L = low-mass line-rich core), while the colored squares represent the sources in the literature (References: HMCs: Bøgelund et al. 2019; Peng et al. 2022; hot corinos: Taquet et al. 2015; Lefloch et al. 2017; Ospina-Zamudio et al. 2018; Jørgensen et al. 2018). The orange areas indicate the relative abundance ranges of molecules. The black dashed lines and the gray dashed lines are linear least-squares fits of this work and all sources, respectively. The fitting results and Pearson correlation coefficients (r) are shown on the top left.

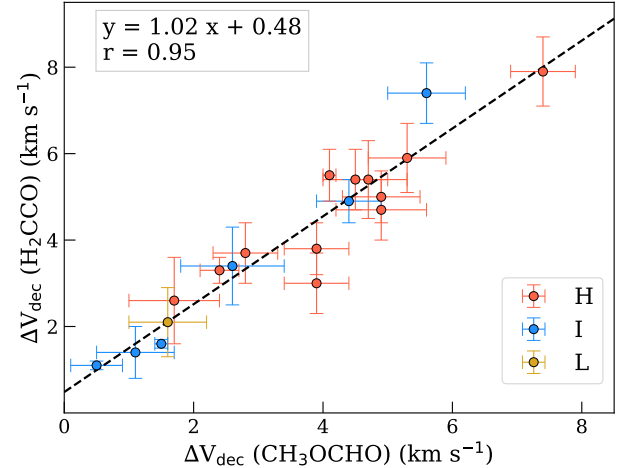
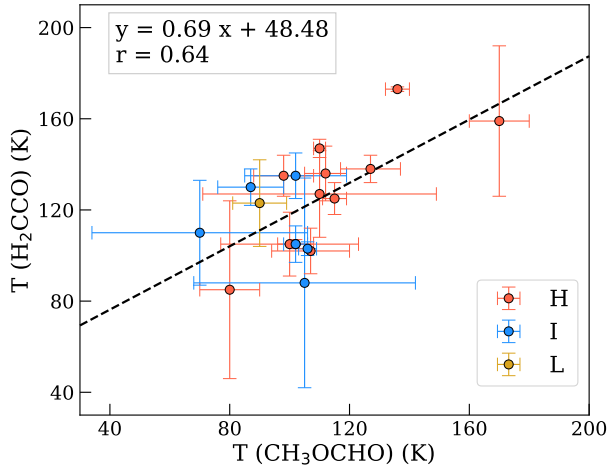
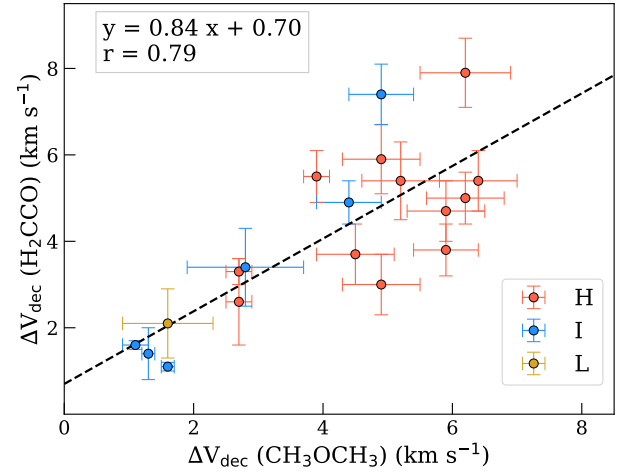
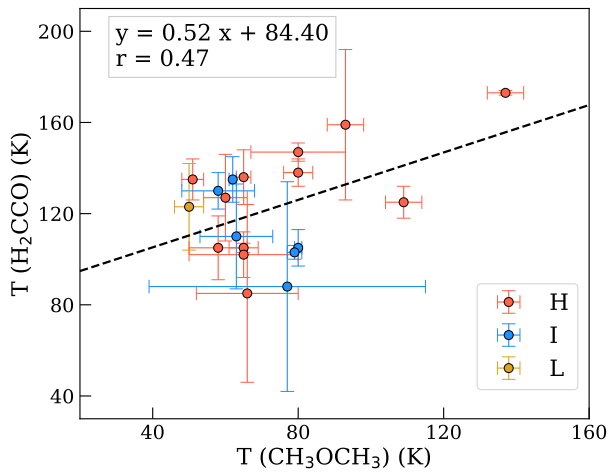
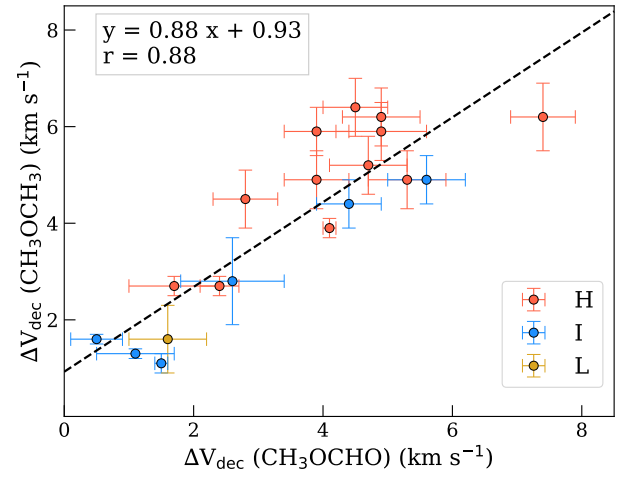
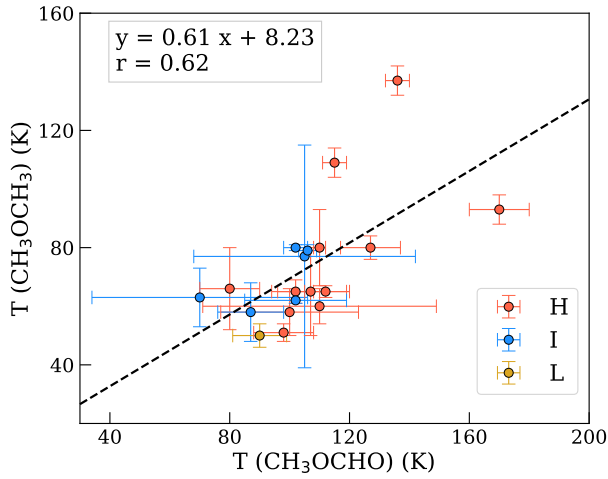


Figure 5. Comparison among the rotation temperatures of CH_3OCHO , CH_3OCH_3 , and H_2CCO . The colored circles represent different types of cores (H = high-mass line-rich core, I = intermediate-mass line-rich core, and L = low-mass line-rich core). The black dashed lines are the linear least-squares fits to the data. The fitting results and Pearson correlation coefficients (r) are shown on the top left.

Figure 6. Comparison among the line widths of CH_3OCHO , CH_3OCH_3 , and H_2CCO . The colored circles represent different types of cores (H = high-mass line-rich core, I = intermediate-mass line-rich core, and L = low-mass line-rich core). The black dashed lines are the linear least-squares fits to the data. The fitting results and Pearson correlation coefficients (r) are shown on the top left.

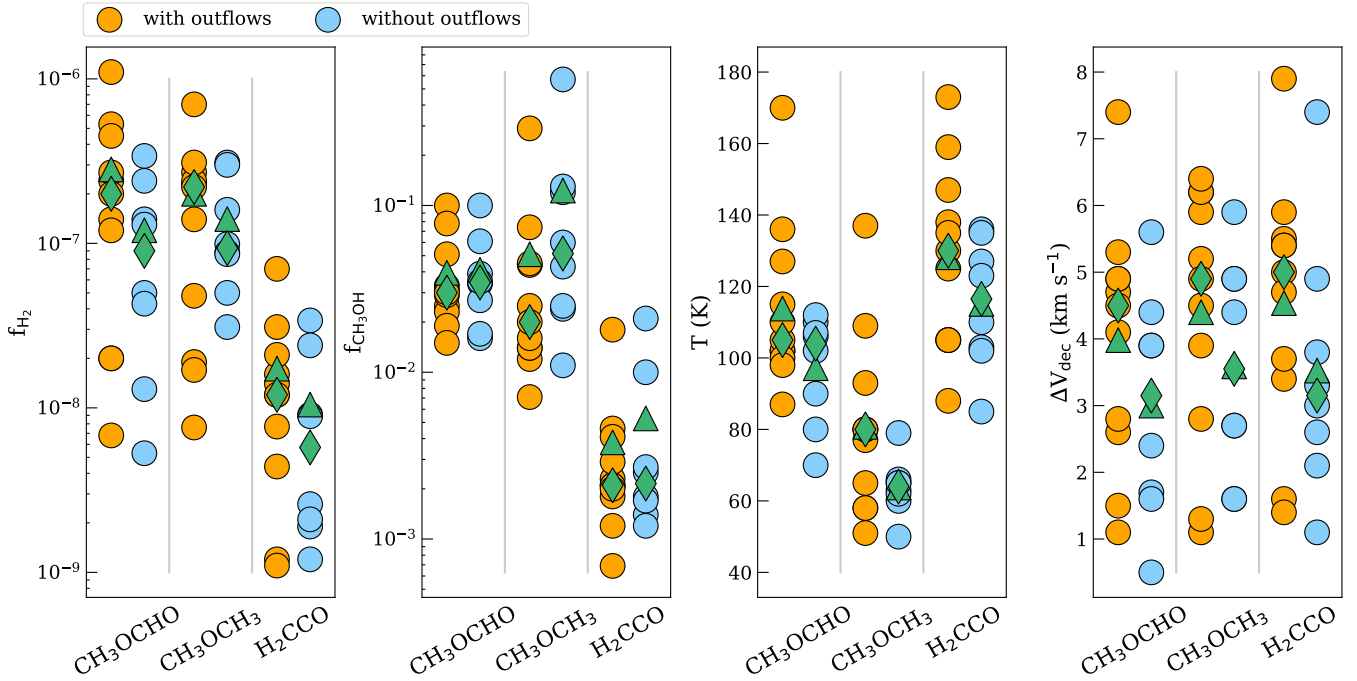
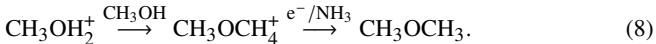


Figure 7. Comparison of molecular abundances relative to H_2 and CH_3OH , rotation temperatures and line widths of the cores with and without detected outflows. The colored circles represent cores with and without outflows. The green triangles represent the averages and the green diamonds represent the medians.

widths of the three molecules tend to be higher where outflows are detected. These results confirm that massive cores and cores with outflows may have richer chemistry (Jørgensen et al. 2020; Ceccarelli et al. 2023).

4.3 Implications for Chemistry

The spatial similarities, abundance correlations and line width correlations of CH_3OCHO , CH_3OCH_3 , and H_2CCO are obvious. We briefly summarize the chemical models of these three molecules below. In gas-phase chemistry, protonated methanol (CH_3OH_2^+) can react with CH_3OH to produce CH_3OCH_3 as follows (Charnley et al. 1995; Taquet et al. 2016; Jørgensen et al. 2020):



Balucani et al. (2015) proposed that CH_3OCH_3 could generate CH_3OCHO in cold gas environments through the following reactions:



where CH_3OCH_3 is a precursor to CH_3OCHO . In the case of grain-surface chemistry, the CH_3OCHO and CH_3OCH_3 follow the reactions (Garrod & Herbst 2006; Garrod et al. 2008):



where methoxide (CH_3O) is the common precursor of CH_3OCHO and CH_3OCH_3 . On the surface of the dust grains, the aldehyde (HCO)

can produce H_2CCO as follows (Charnley et al. 2001; Charnley & Rodgers 2005; Krasnokutski et al. 2017):



where HCO is the common precursor of CH_3OCHO and H_2CCO through Eq. (10) (12). The spatial similarities, abundance correlations, and line width correlations of CH_3OCHO , CH_3OCH_3 , and H_2CCO , combined with chemical models, suggest that three molecules are chemically related. Taquet et al. (2016) predicted the abundances of CH_3OCH_3 relative to H_2 to be $\sim 10^{-7}$ and relative to CH_3OH to be $\sim 10^{-2}$ using reaction (8). Our observed abundances of CH_3OCH_3 relative to H_2 and CH_3OH are consistent with this prediction. Garrod et al. (2022) showed a chemical network that includes reactions (8), (9), (10), (11), and (13) to predict the abundances of CH_3OCHO , CH_3OCH_3 , and H_2CCO . The three warm-up timescales of 5×10^4 years (fast), 2×10^5 years (medium), and 1×10^6 years (slow) were employed in their models. At the medium timescale, the predicted abundances relative to H_2 are $\sim 10^{-7}$ for CH_3OCHO and CH_3OCH_3 , $\sim 10^{-8}$ for H_2CCO , and relative to CH_3OH are $\sim 10^{-2}$ for CH_3OCHO and CH_3OCH_3 , $\sim 10^{-3}$ for H_2CCO . Our observed abundances of the three molecules relative to H_2 and CH_3OH are consistent with the medium timescale predictions. In conclusion, our observed abundances of the three molecules support both grain-surface and gas-phase chemical pathways for the production of CH_3OCHO and CH_3OCH_3 , and grain-surface chemical pathways for the production of H_2CCO .

5 CONCLUSIONS

We have analyzed the spectra of 11 high-mass star-forming regions obtained by ALMA band 7 observations, and studied the correlations of complex organic molecules CH₃OCHO and CH₃OCH₃ as well as an important precursor of complex organic molecules H₂CCO. We summarize the main results in the following:

1. CH₃OCHO, CH₃OCH₃, and H₂CCO lines were detected in 19 line-rich cores from 9 out of 11 high-mass star-forming regions. At our higher spatial resolution observations, some of the hot molecular cores found in previous observations are revealed to actually host multiple line-rich cores with different masses.

2. The integrated intensity maps of the 9 high-mass star-forming regions show that the emission peaks of the three molecules are consistent, and the spatial distribution of the molecules is similar. The emissions of the three molecules in the 9 high-mass star-forming regions are primarily distributed around intense continuum emission.

3. The abundances relative to H₂ and CH₃OH, and line widths of the three molecules show obvious correlations in the 19 dense cores. The abundance correlations of the three molecules relative to H₂ and CH₃OH in other hot molecular cores and hot corinos agree with the results in our observations. The molecular abundances of CH₃OCHO and CH₃OCH₃ are rather similar, while the molecular abundances of H₂CCO are one order of magnitude lower.

4. The abundances relative to H₂, temperatures and line widths of the three molecules tend to be higher in the cores with higher mass and with outflows. This confirms that massive cores and cores with outflows may have richer chemistry.

5. The spatial similarities, abundance correlations, and line width correlations of CH₃OCHO, CH₃OCH₃, and H₂CCO, combined with chemical models, suggest that three molecules are chemically related. Our results suggest that both grain-surface and gas-phase chemical pathways can be responsible for producing CH₃OCHO and CH₃OCH₃, while H₂CCO should be produced by grain-surface chemical pathways.

ACKNOWLEDGEMENTS

This paper makes use of the following ALMA data: ADS/JAO.ALMA#2017.1.00545.S. ALMA is a partnership of ESO (representing its member states), NSF (USA), and NINS (Japan), together with NRC (Canada), MOST and ASIAA (Taiwan), and KASI (Republic of Korea), in cooperation with the Republic of Chile. The Joint ALMA Observatory is operated by ESO, AUI/NRAO, and NAOJ. This work has been supported by National Key R&D Program of China (No. 2022YFA1603101), and by NSFC through the grants No. 12033005, No. 12073061, No. 12122307, and No. 12103045. S.-L. Qin thanks the Xinjiang Uygur Autonomous Region of China for their support through the Tianchi Program. MYT acknowledges the support by NSFC through grants No.12203011, and Yunnan provincial Department of Science and Technology through grant No.202101BA070001-261. T. Zhang thanks the student's exchange program of the Collaborative Research Centre 956, funded by the Deutsche Forschungsgemeinschaft (DFG).

DATA AVAILABILITY

The data underlying this article are available in the ALMA archive.

REFERENCES

- Agúndez M., Marcelino N., Cernicharo J., Roueff E., Tafalla M., 2019, *A&A*, **625**, A147
- Bacmann A., Taquet V., Faure A., Kahane C., Ceccarelli C., 2012, *A&A*, **541**, L12
- Balucani N., Ceccarelli C., Taquet V., 2015, *MNRAS*, **449**, L16
- Baug T., et al., 2020, *ApJ*, **890**, 44
- Belloche A., Müller H. S. P., Menten K. M., Schilke P., Comito C., 2013, *A&A*, **559**, A47
- Bergner J. B., Öberg K. I., Garrod R. T., Graninger D. M., 2017, *ApJ*, **841**, 120
- Bergner J. B., Martín-Doménech R., Öberg K. I., Jørgensen J. K., Artur de la Villarmois E., Brinch C., 2019, *ACS Earth and Space Chemistry*, **3**, 1564
- Bianchi E., et al., 2019, *MNRAS*, **483**, 1850
- Biver N., Bockelée-Morvan D., 2019, *ACS Earth and Space Chemistry*, **3**, 1550
- Bøgelund E. G., Barr A. G., Taquet V., Ligterink N. F. W., Persson M. V., Hogerheijde M. R., van Dishoeck E. F., 2019, *A&A*, **628**, A2
- Bottinelli S., et al., 2004, *ApJ*, **615**, 354
- Bottinelli S., Ceccarelli C., Williams J. P., Lefloch B., 2007, *A&A*, **463**, 601
- Cazaux S., Tielens A. G. G. M., Ceccarelli C., Castets A., Wakelam V., Caux E., Parise B., Teyssier D., 2003, *ApJ*, **593**, L51
- Ceccarelli C., et al., 2023, in Inutsuka S., Aikawa Y., Muto T., Tomida K., Tamura M., eds, *Astronomical Society of the Pacific Conference Series* Vol. 534, *Protostars and Planets VII*. p. 379
- Cernicharo J., Marcelino N., Roueff E., Gerin M., Jiménez-Escobar A., Muñoz Caro G. M., 2012, *ApJ*, **759**, L43
- Charnley S. B., Rodgers S. D., 2005, in Lis D. C., Blake G. A., Herbst E., eds, Vol. 231, *Astrochemistry: Recent Successes and Current Challenges*. pp 237–246, doi:10.1017/S174392130600723X
- Charnley S. B., Kress M. E., Tielens A. G. G. M., Millar T. J., 1995, *ApJ*, **448**, 232
- Charnley S. B., Ehrenfreund P., Kuan Y. J., 2001, *Spectrochimica Acta Part A: Molecular Spectroscopy*, **57**, 685
- Chen Y., et al., 2023, *A&A*, **678**, A137
- Chen L., et al., 2024, *ApJ*, **962**, 13
- Coletta A., Fontani F., Rivilla V. M., Mininni C., Colzi L., Sánchez-Monge Á., Beltrán M. T., 2020, *A&A*, **641**, A54
- Crockett N. R., Bergin E. A., Neill J. L., Favre C., Blake G. A., Herbst E., Anderson D. E., Hassel G. E., 2015, *ApJ*, **806**, 239
- Csengeri T., Belloche A., Bontemps S., Wyrowski F., Menten K. M., Bouscasse L., 2019, *A&A*, **632**, A57
- Duley W. W., Williams D. A., 1984, *Interstellar chemistry*
- Favre C., Despois D., Brouillet N., Baudry A., Combes F., Guélin M., Wootten A., Włodarczak G., 2011, *A&A*, **532**, A32
- Fedoseev G., Qasim D., Chuang K.-J., Ioppolo S., Lamberts T., van Dishoeck E. F., Linnartz H., 2022, *ApJ*, **924**, 110
- Feng S., Beuther H., Henning T., Semenov D., Palau A., Mills E. A. C., 2015, *A&A*, **581**, A71
- Frau P., et al., 2010, *ApJ*, **723**, 1665
- Friedel D. N., Snyder L. E., 2008, *ApJ*, **672**, 962
- Fuente A., et al., 2014, *A&A*, **568**, A65
- Garrod R. T., Herbst E., 2006, *A&A*, **457**, 927
- Garrod R. T., Widicus Weaver S. L., Herbst E., 2008, *ApJ*, **682**, 283
- Garrod R. T., Jin M., Matis K. A., Jones D., Willis E. R., Herbst E., 2022, *ApJS*, **259**, 1
- Gieser C., et al., 2021, *A&A*, **648**, A66
- Hasegawa T. I., Herbst E., Leung C. M., 1992, *ApJS*, **82**, 167
- Herbst E., van Dishoeck E. F., 2009, *ARA&A*, **47**, 427
- Hudson R. L., Loeffler M. J., 2013, *ApJ*, **773**, 109
- Jaber A. A., Ceccarelli C., Kahane C., Caux E., 2014, *ApJ*, **791**, 29
- Jørgensen J. K., et al., 2018, *A&A*, **620**, A170
- Jørgensen J. K., Belloche A., Garrod R. T., 2020, *ARA&A*, **58**, 727
- Kauffmann J., Bertoldi F., Bourke T. L., Evans N. J. I., Lee C. W., 2008, *A&A*, **487**, 993
- Krasnokutski S. A., et al., 2017, *ApJ*, **847**, 89

- Lefloch B., Ceccarelli C., Codella C., Favre C., Podio L., Vastel C., Viti S., Bachiller R., 2017, *MNRAS*, **469**, L73
- Lis D. C., Carlstrom J. E., Keene J., 1991, *ApJ*, **380**, 429
- Liu T., et al., 2016, *ApJ*, **829**, 59
- Liu T., et al., 2020, *MNRAS*, **496**, 2790
- Liu H.-L., et al., 2022, *MNRAS*, **511**, 501
- López-Gallifa Á., et al., 2024, *MNRAS*, **529**, 3244
- Maity S., Kaiser R. I., Jones B. M., 2014, *ApJ*, **789**, 36
- Maret S., et al., 2004, *A&A*, **416**, 577
- McMullin J. P., Waters B., Schiebel D., Young W., Golap K., 2007, in Shaw R. A., Hill F., Bell D. J., eds, *Astronomical Society of the Pacific Conference Series Vol. 376, Astronomical Data Analysis Software and Systems XVI*, p. 127
- Möller T., Bernst I., Panoglou D., Muders D., Ossenkopf V., Röllig M., Schilke P., 2013, *A&A*, **549**, A21
- Möller T., Endres C., Schilke P., 2017, *A&A*, **598**, A7
- Müller H. S. P., Thorwirth S., Roth D. A., Winnewisser G., 2001, *A&A*, **370**, L49
- Müller H. S. P., Schlöder F., Stutzki J., Winnewisser G., 2005, *Journal of Molecular Structure*, **742**, 215
- Nummelin A., Bergman P., Hjalmarsen Å., Friberg P., Irvine W. M., Millar T. J., Ohishi M., Saito S., 2000, *ApJS*, **128**, 213
- Ospina-Zamudio J., Lefloch B., Ceccarelli C., Kahane C., Favre C., López-Sepulcre A., Montarges M., 2018, *A&A*, **618**, A145
- Ossenkopf V., Henning T., 1994, *A&A*, **291**, 943
- Palau A., et al., 2011, *ApJ*, **743**, L32
- Peng Y., et al., 2022, *MNRAS*, **512**, 4419
- Pickett H. M., Poynter R. L., Cohen E. A., Delitsky M. L., Pearson J. C., Müller H. S. P., 1998, *J. Quant. Spectrosc. Radiative Transfer*, **60**, 883
- Qin S.-L., Wu Y., Huang M., Zhao G., Li D., Wang J.-J., Chen S., 2010, *ApJ*, **711**, 399
- Qin S.-L., Schilke P., Wu J., Wu Y., Liu T., Liu Y., Sánchez-Monge Á., 2015, *ApJ*, **803**, 39
- Qin S.-L., et al., 2022, *MNRAS*, **511**, 3463
- Requena-Torres M. A., Martín-Pintado J., Rodríguez-Franco A., Martín S., Rodríguez-Fernández N. J., de Vicente P., 2006, *A&A*, **455**, 971
- Requena-Torres M. A., Martín-Pintado J., Martín S., Morris M. R., 2008, *ApJ*, **672**, 352
- Rivilla V. M., Beltrán M. T., Cesaroni R., Fontani F., Codella C., Zhang Q., 2017, *A&A*, **598**, A59
- Ruud M., Loison J. C., Hickson K. M., Gratier P., Hersant F., Wakelam V., 2015, *MNRAS*, **447**, 4004
- Ruffle D. P., Herbst E., 2000, *MNRAS*, **319**, 837
- Ruiterkamp R., Charnley S. B., Butner H. M., Huang H. C., Rodgers S. D., Kuan Y. J., Ehrenfreund P., 2007, *Ap&SS*, **310**, 181
- Sánchez-Monge Á., Palau A., Estalella R., Kurtz S., Zhang Q., Di Francesco J., Shepherd D., 2010, *ApJ*, **721**, L107
- Taquet V., López-Sepulcre A., Ceccarelli C., Neri R., Kahane C., Charnley S. B., 2015, *ApJ*, **804**, 81
- Taquet V., Wirstrom E. S., Charnley S. B., 2016, *ApJ*, **821**, 46
- Vasyunin A. I., Herbst E., 2013, *ApJ*, **769**, 34
- Xu F., et al., 2024, *ApJS*, **270**, 9
- Yan Y. T., et al., 2019, *ApJ*, **877**, 154
- Zhang C., et al., 2023, *MNRAS*, **520**, 3245
- van 't Hoff M. L. R., Bergin E. A., Jørgensen J. K., Blake G. A., 2020, *ApJ*, **897**, L38

APPENDIX B: MOLECULAR TRANSITIONS

The rotational transitions of the three molecules detected in 19 dense cores are shown in Table B1. The molecular parameters are taken from the JPL catalogue for CH₃OCHO lines and the CDMS catalogue for CH₃OCH₃ and H₂CCO lines. Due to internal rotation, the CH₃OCHO rotational levels split into two substates A and E, while the CH₃OCH₃ rotational levels split into four substates AA, EE, EA, and AE.

APPENDIX C: MOLECULAR EMISSION

We compare the molecular emissions of CH₃OCHO with different energy level transitions. The integrated intensity maps of CH₃OCHO at 342572 MHz ($E_u = 81$ K) and at 342359 MHz ($E_u = 269$ K) in 9 high-mass star-forming regions are shown in Figure C1. In the 9 high-mass star-forming regions, there is no difference in the spatial emission between the different energy level transitions of CH₃OCHO.

This paper has been typeset from a $\text{\TeX}/\text{\LaTeX}$ file prepared by the author.

APPENDIX A: SPECTRA OF LINE-RICH CORES

The spectra and optical depths of the three molecules detected in the 19 line-rich cores are shown in Figure 1 and Figure A1.

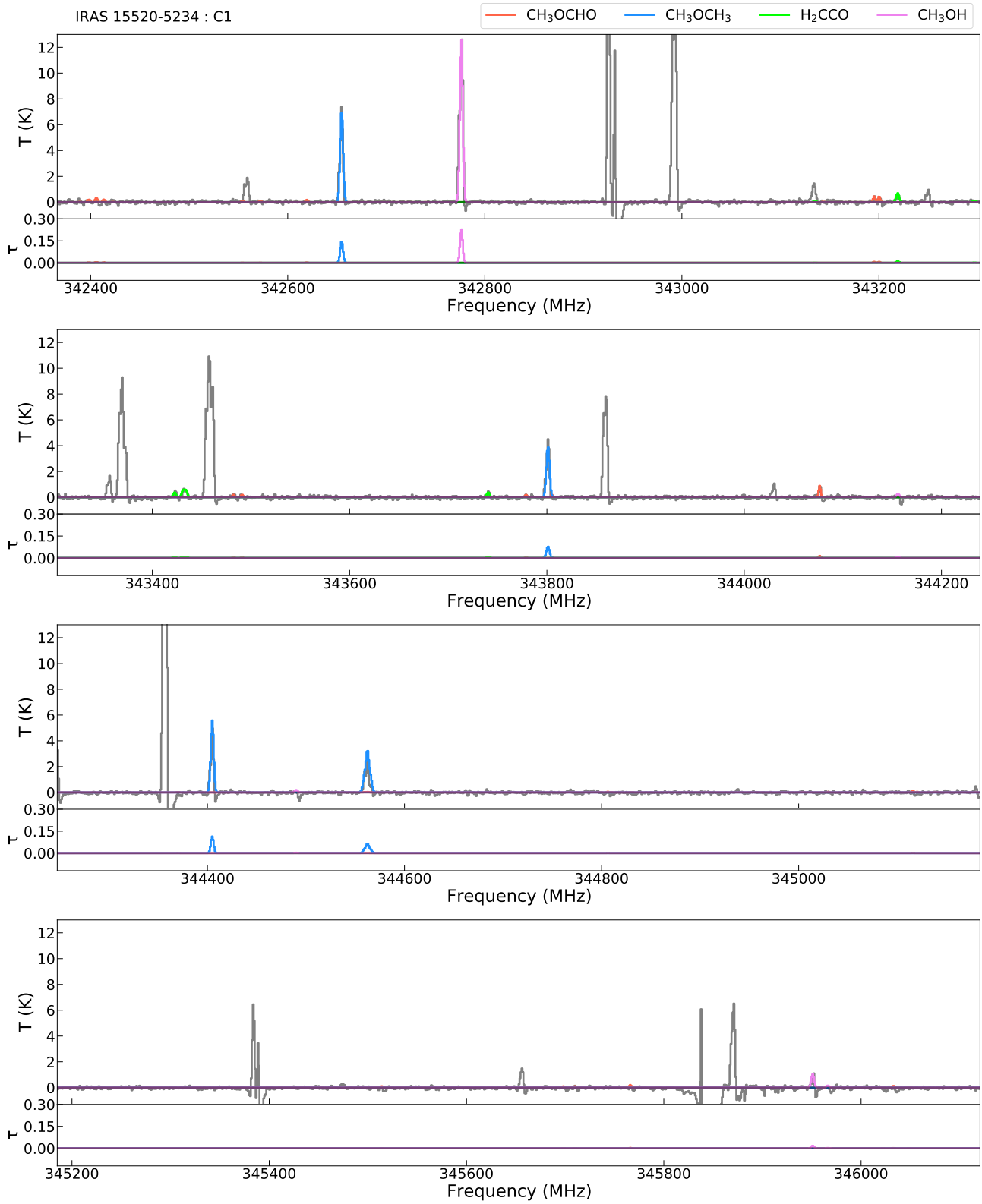
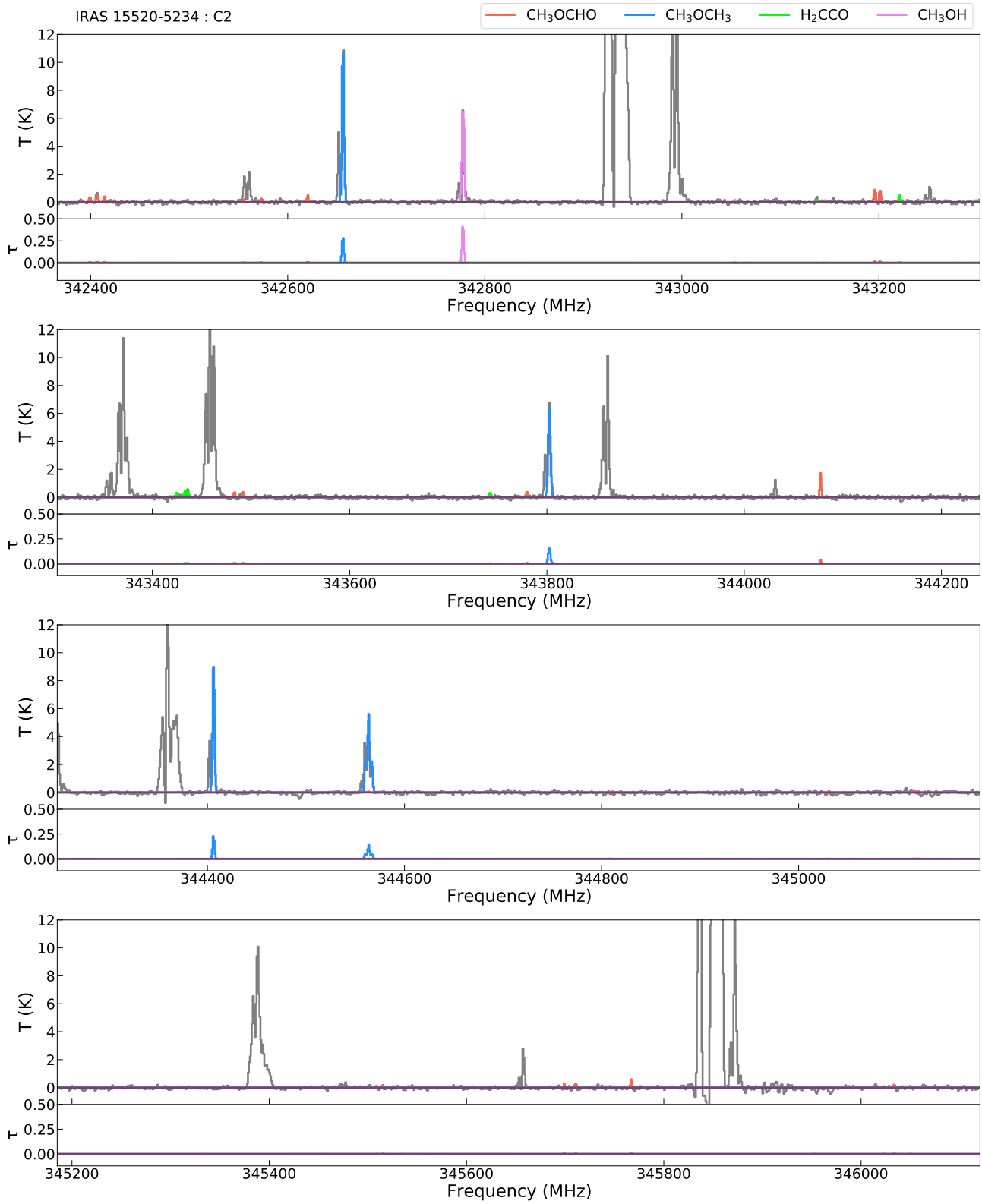


Figure A1. Same as Figure 1, but for the other 18 line-rich cores.

Figure A1. – *continued*

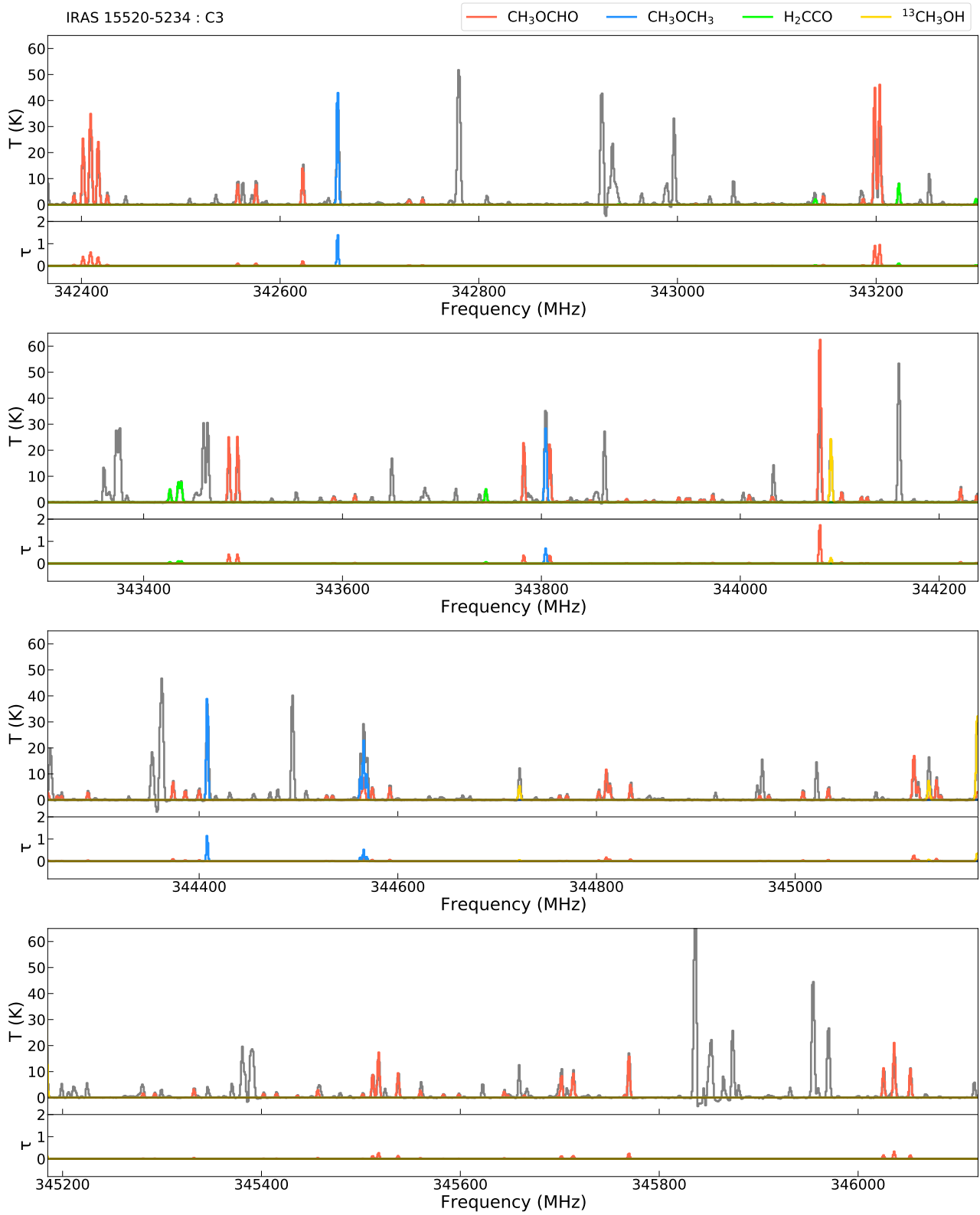


Figure A1. – continued

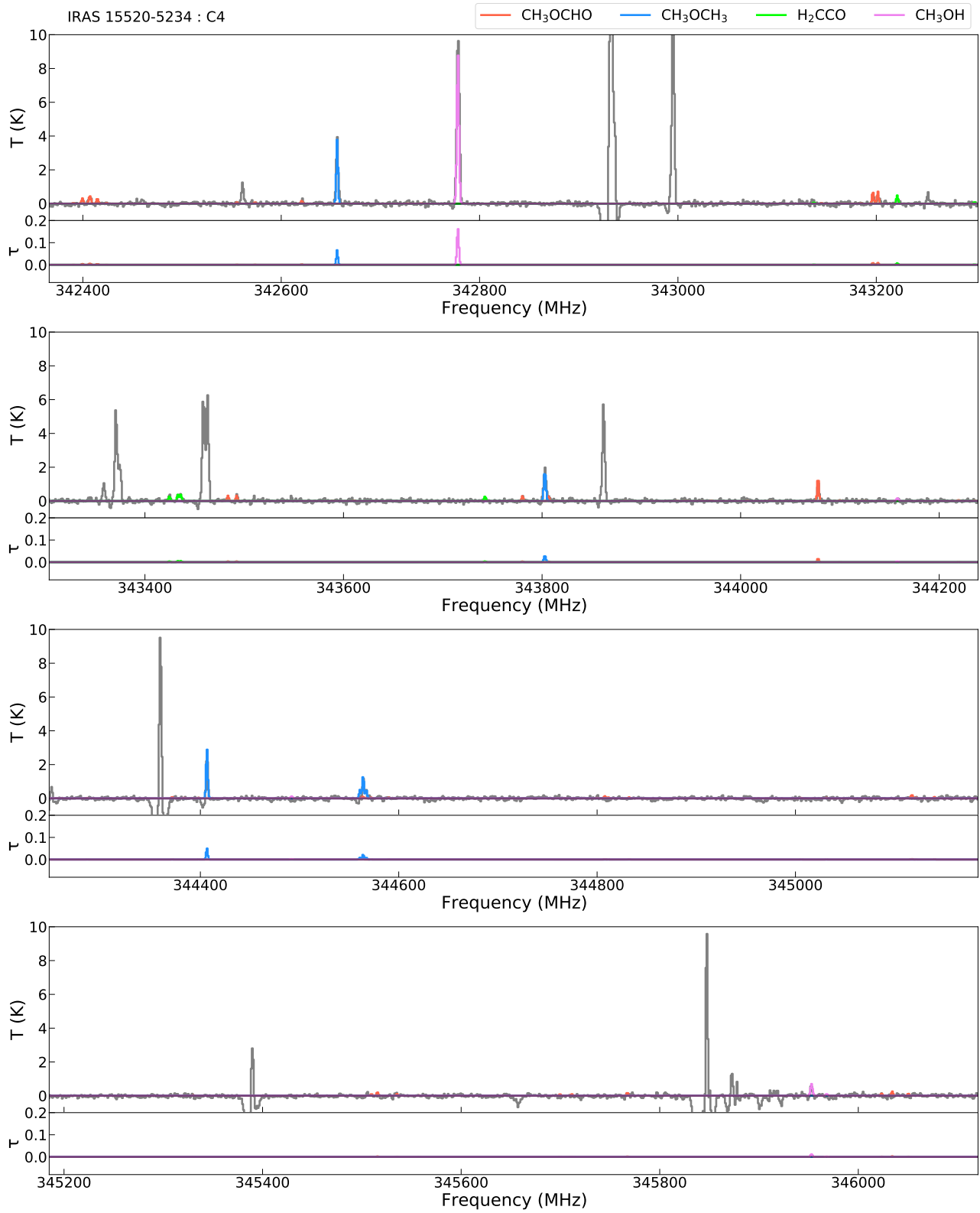
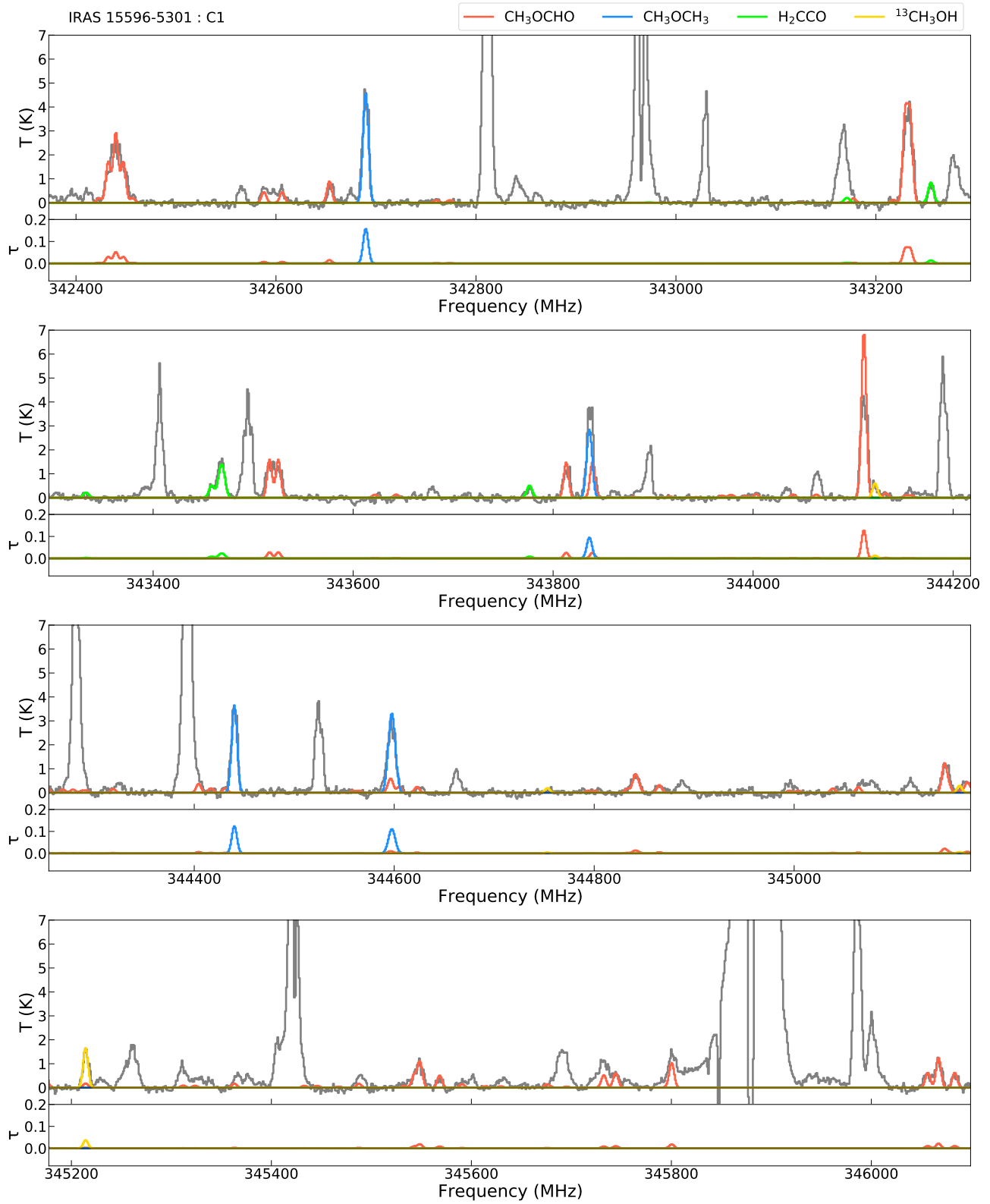
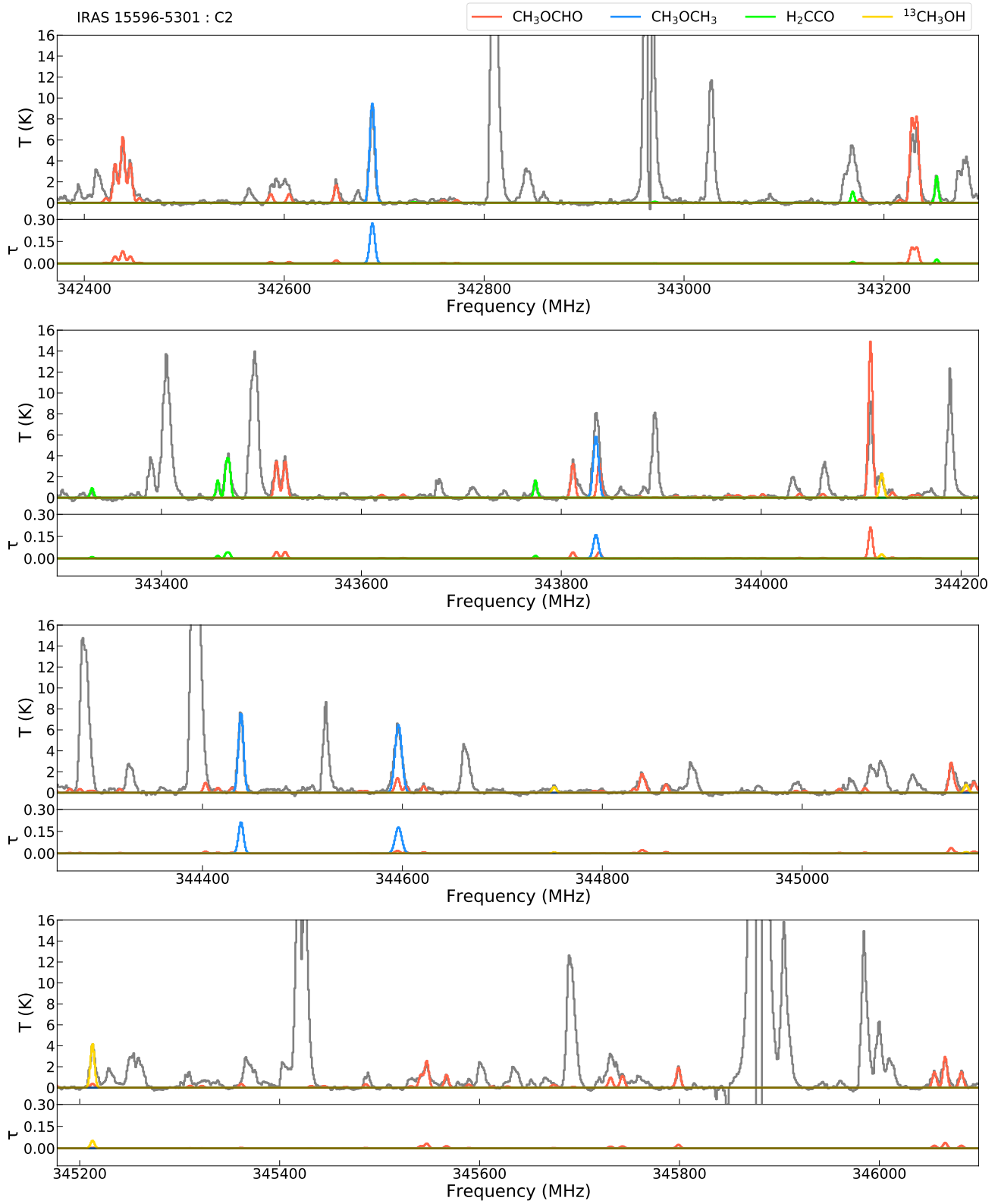


Figure A1. – continued





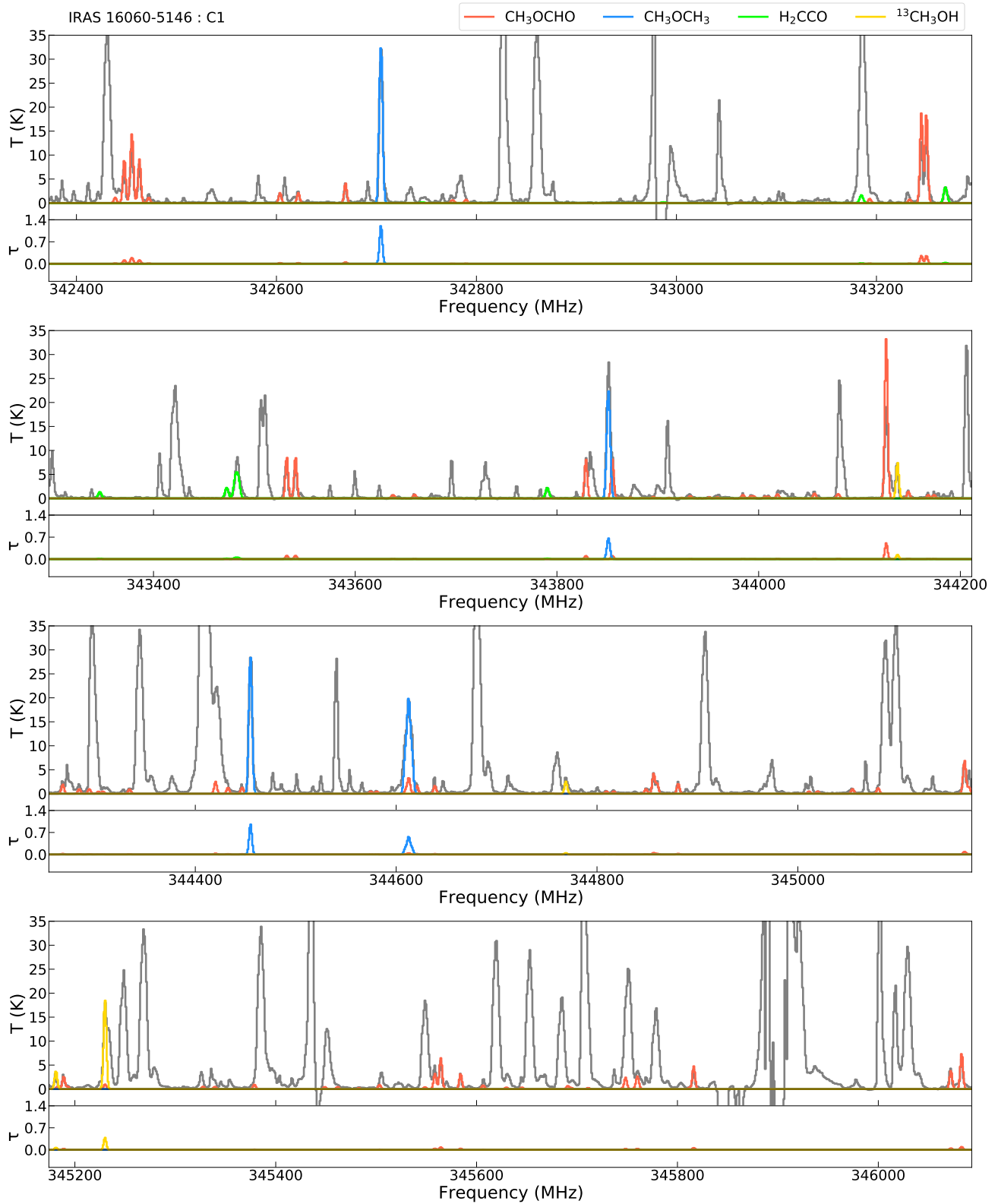
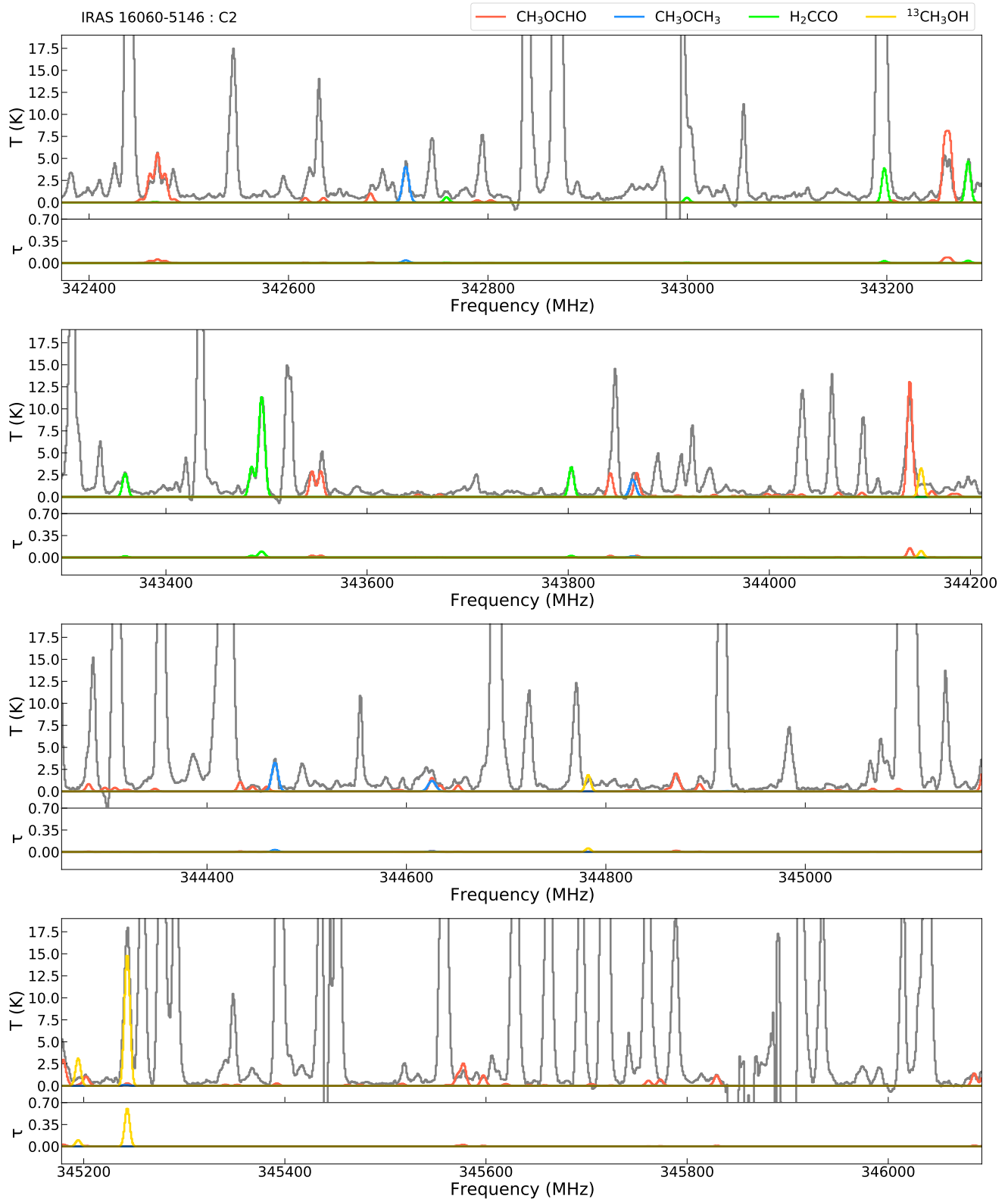


Figure A1. – continued

Figure A1. – *continued*

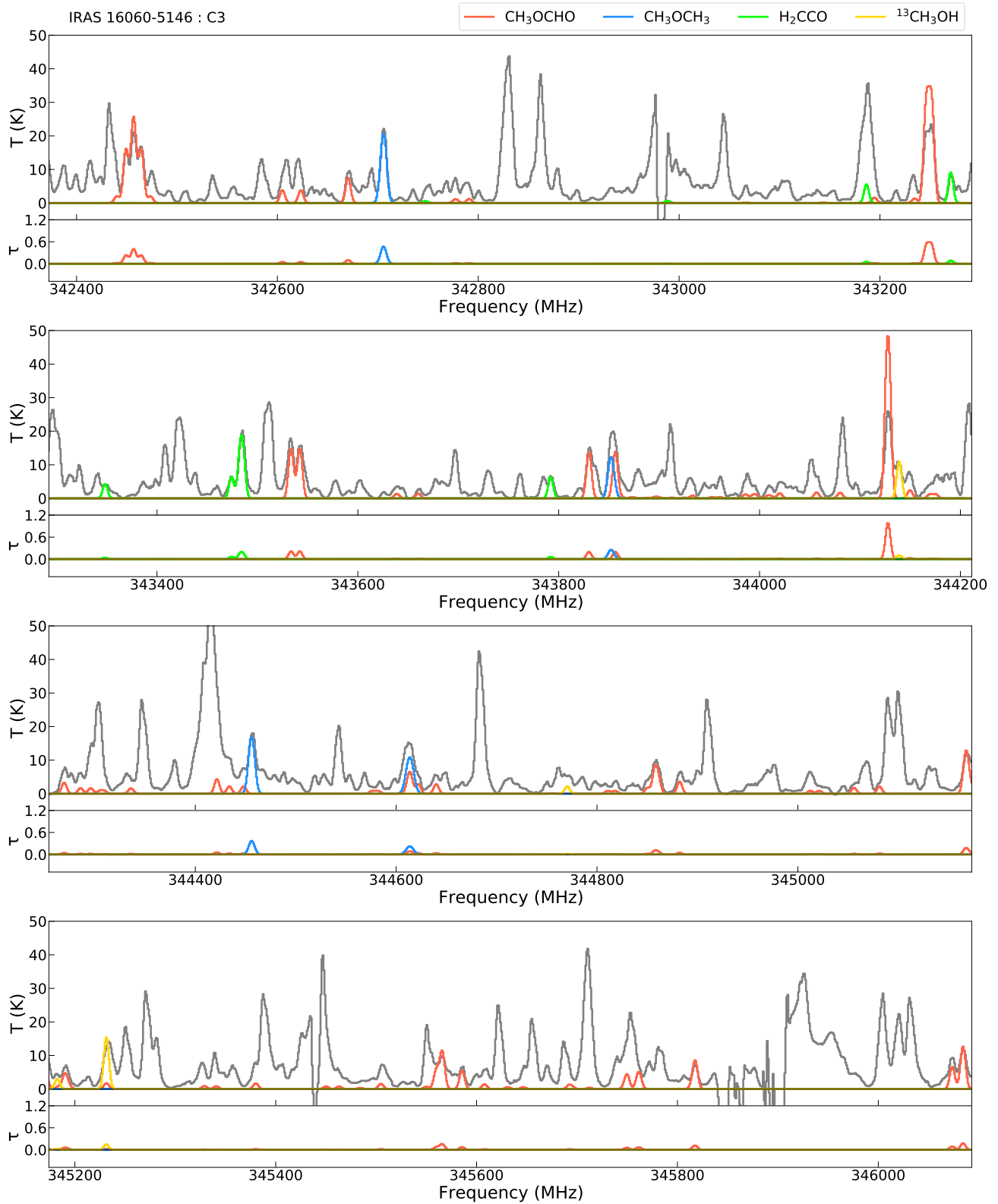
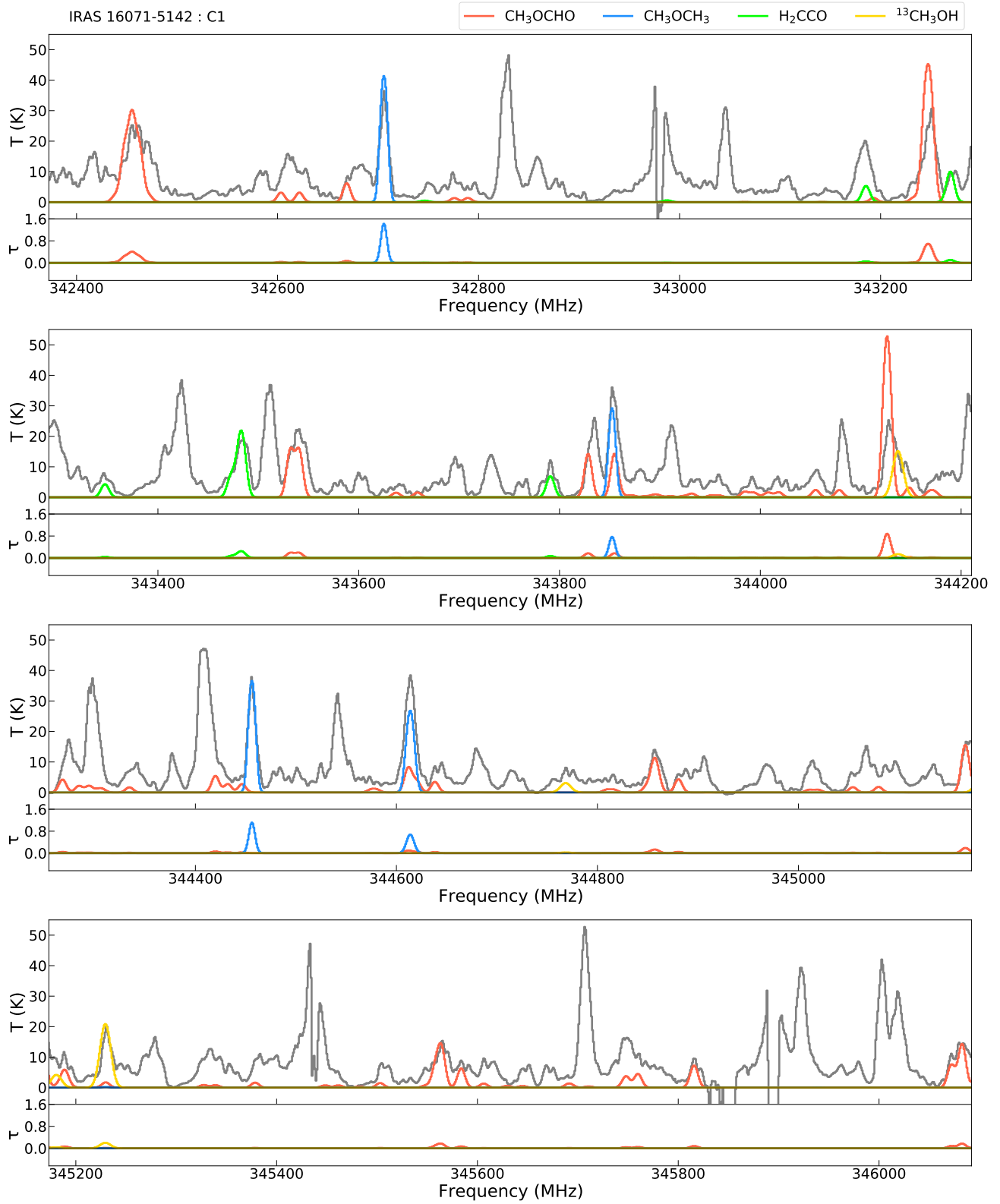
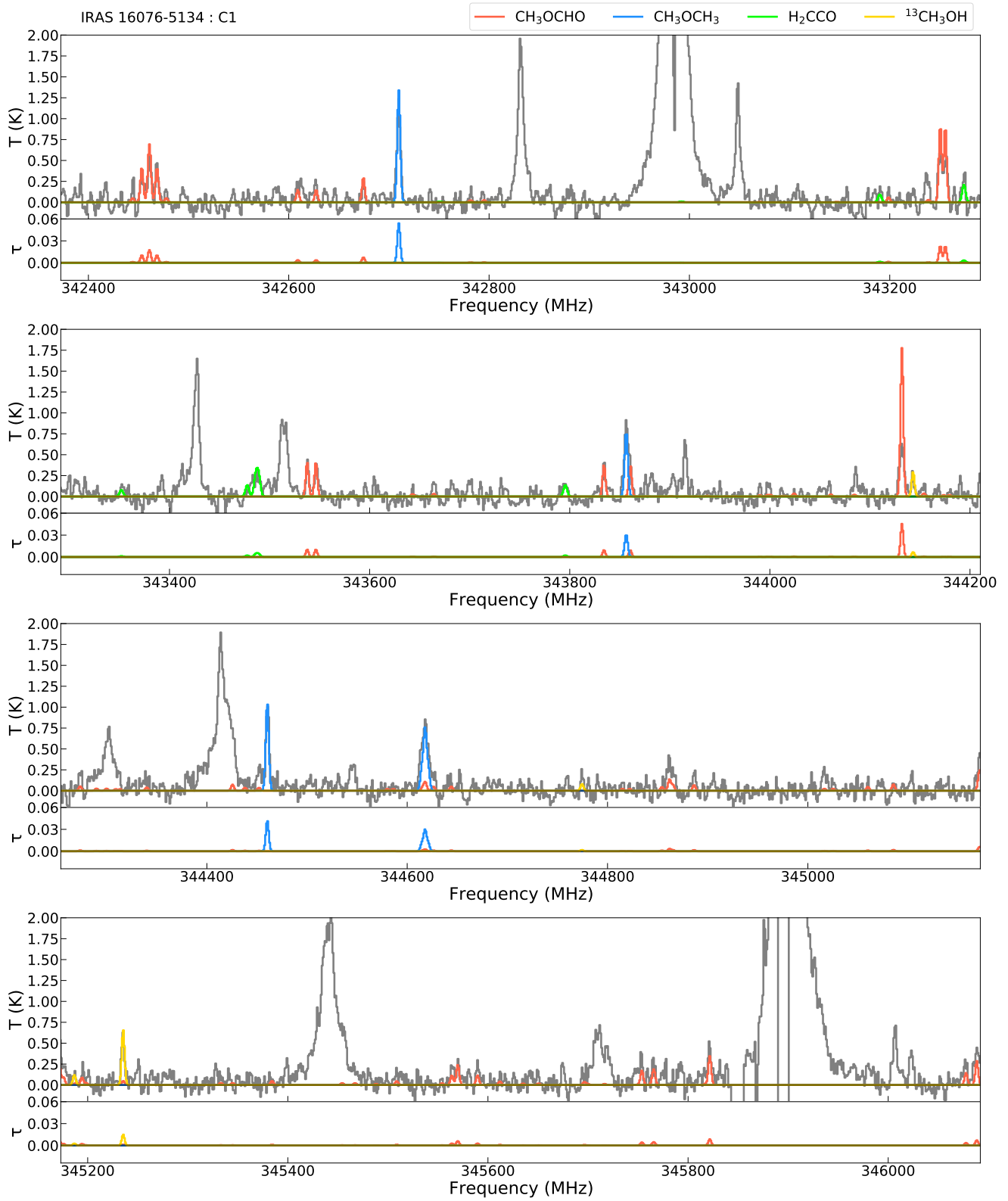
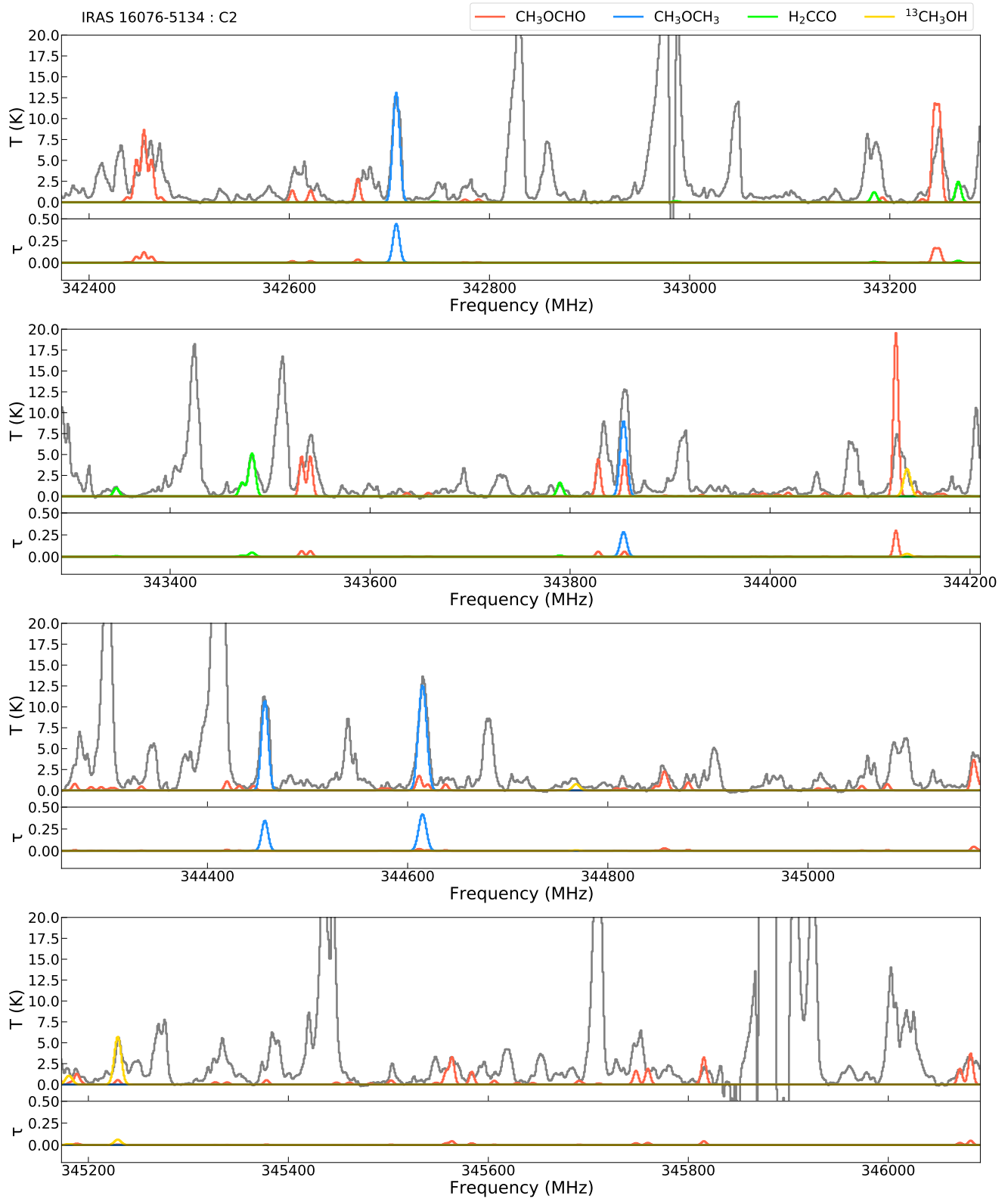
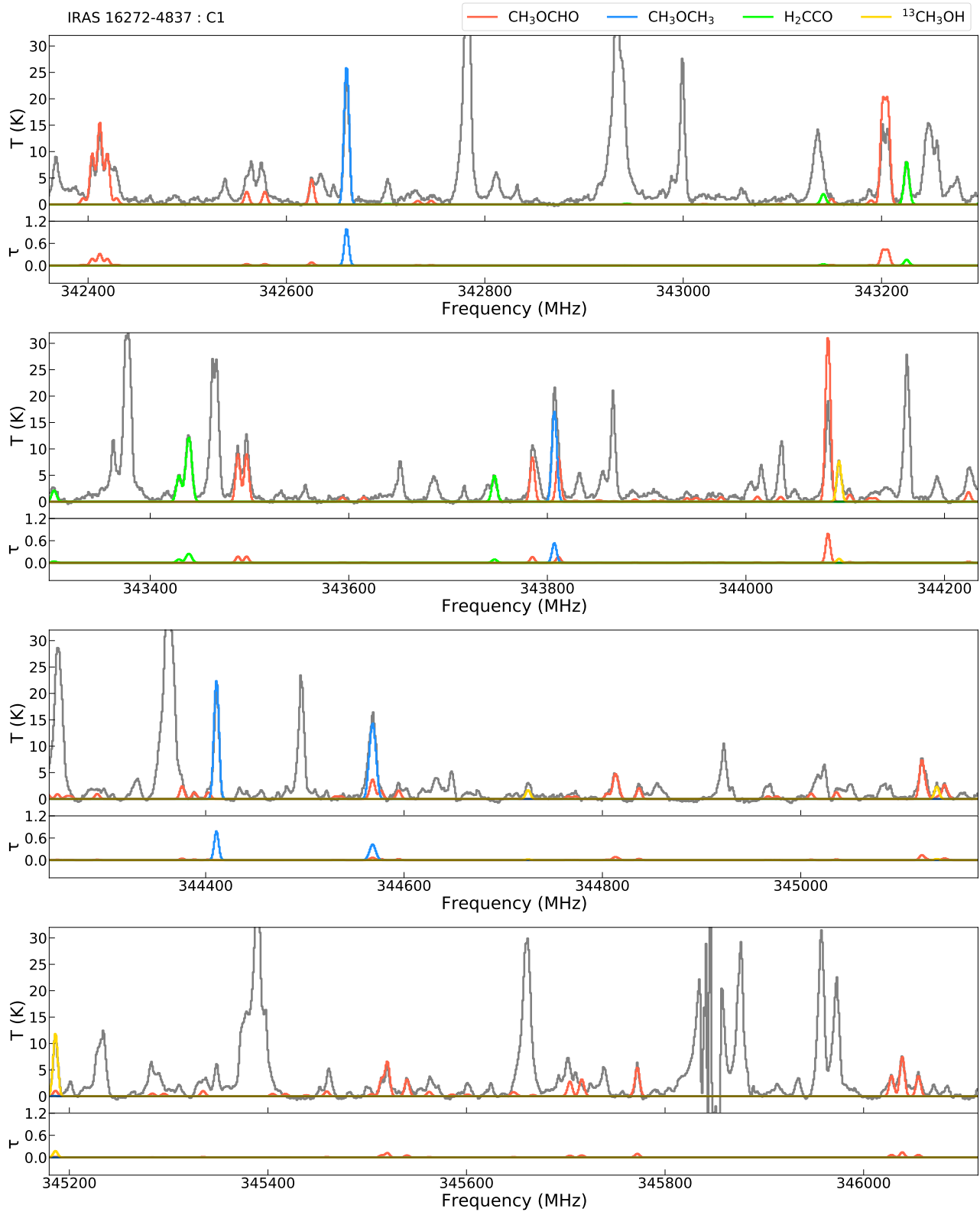


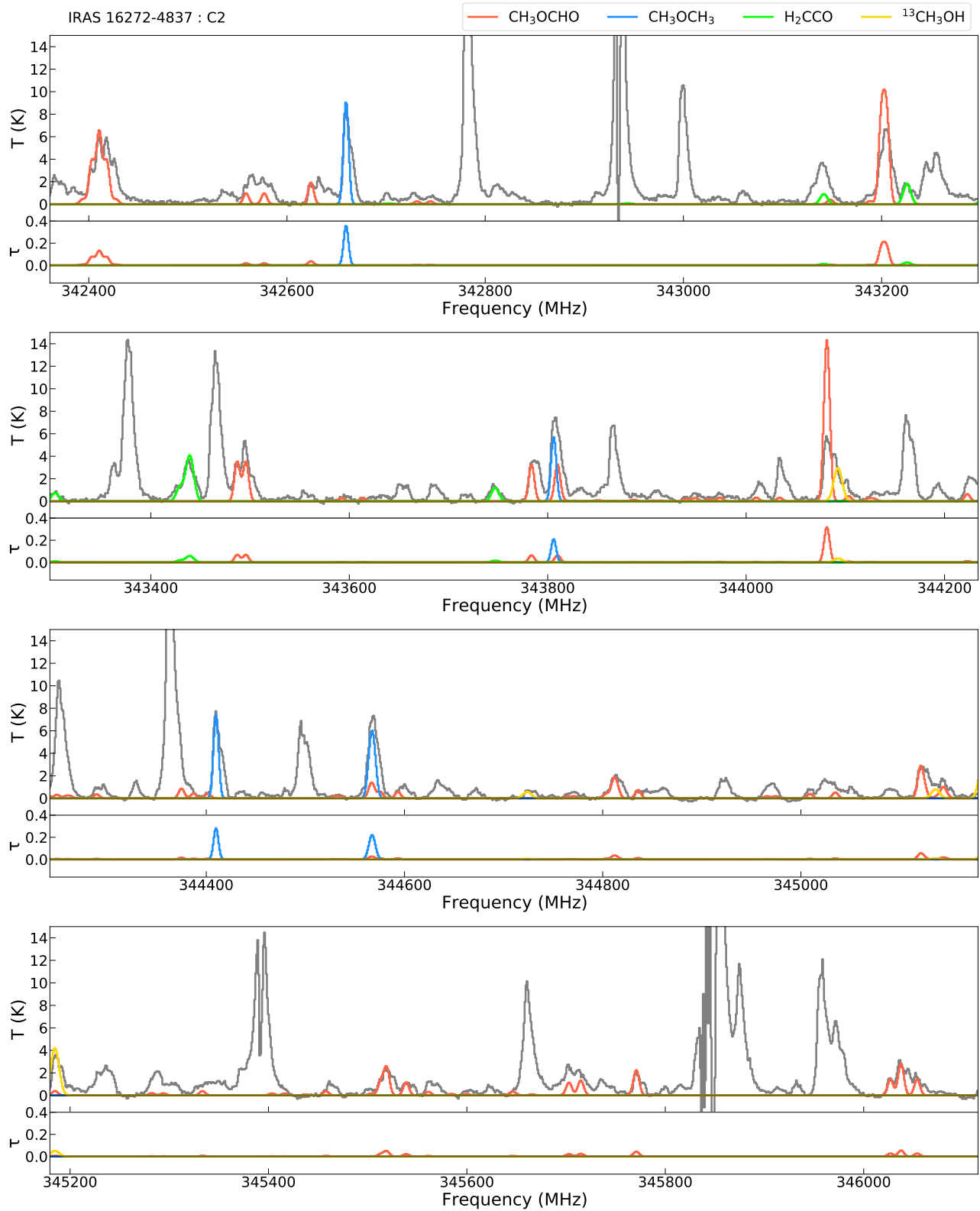
Figure A1. – continued

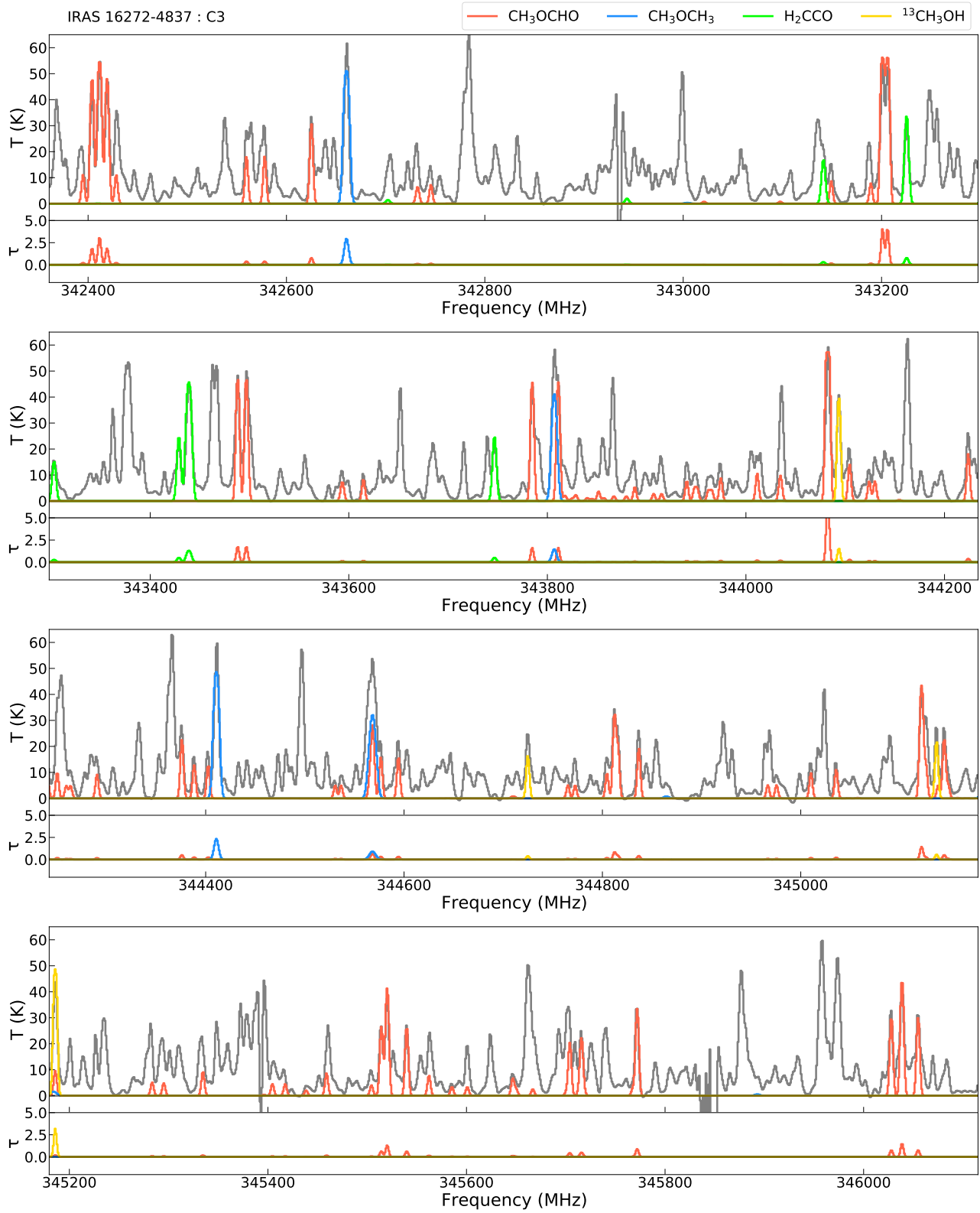


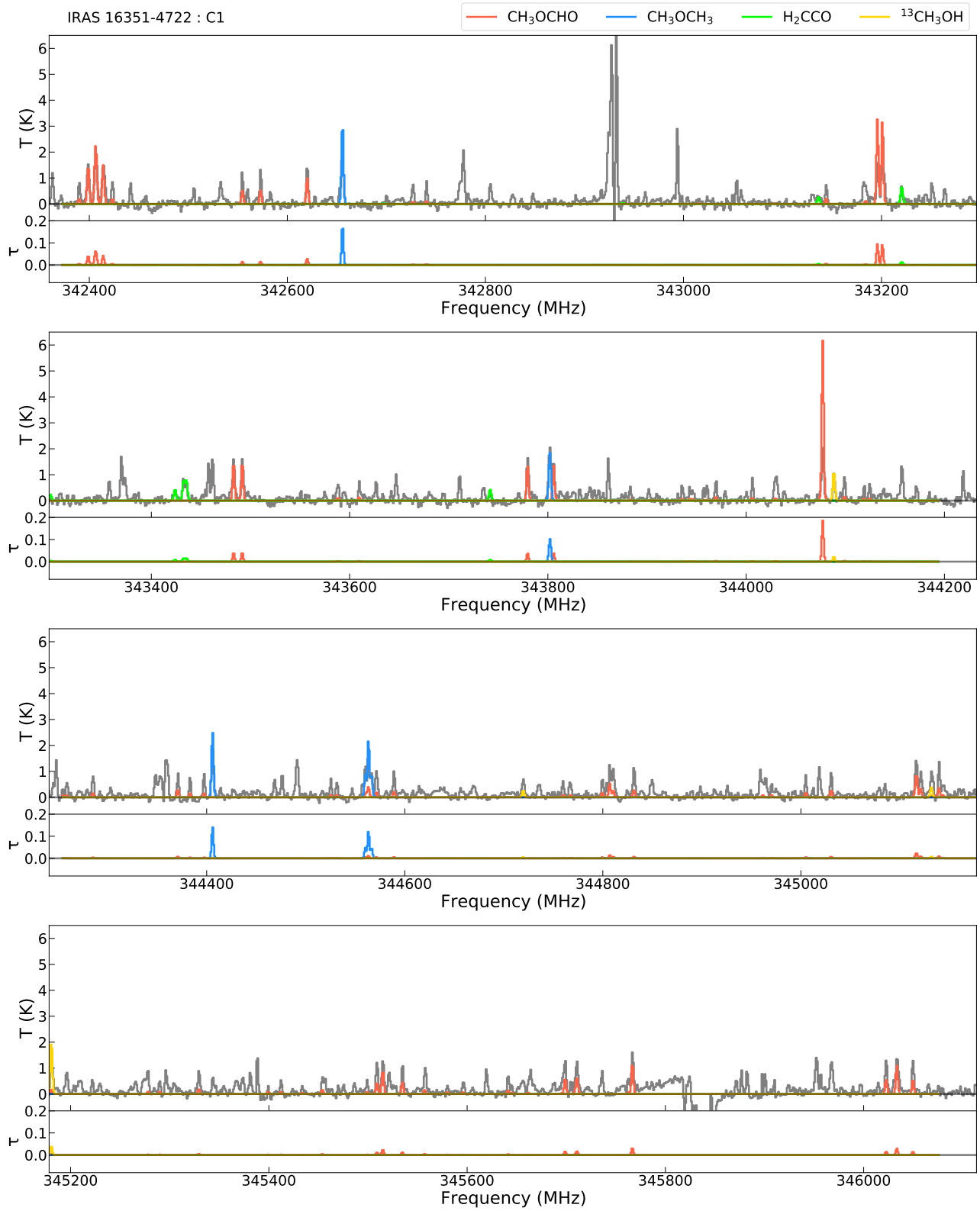


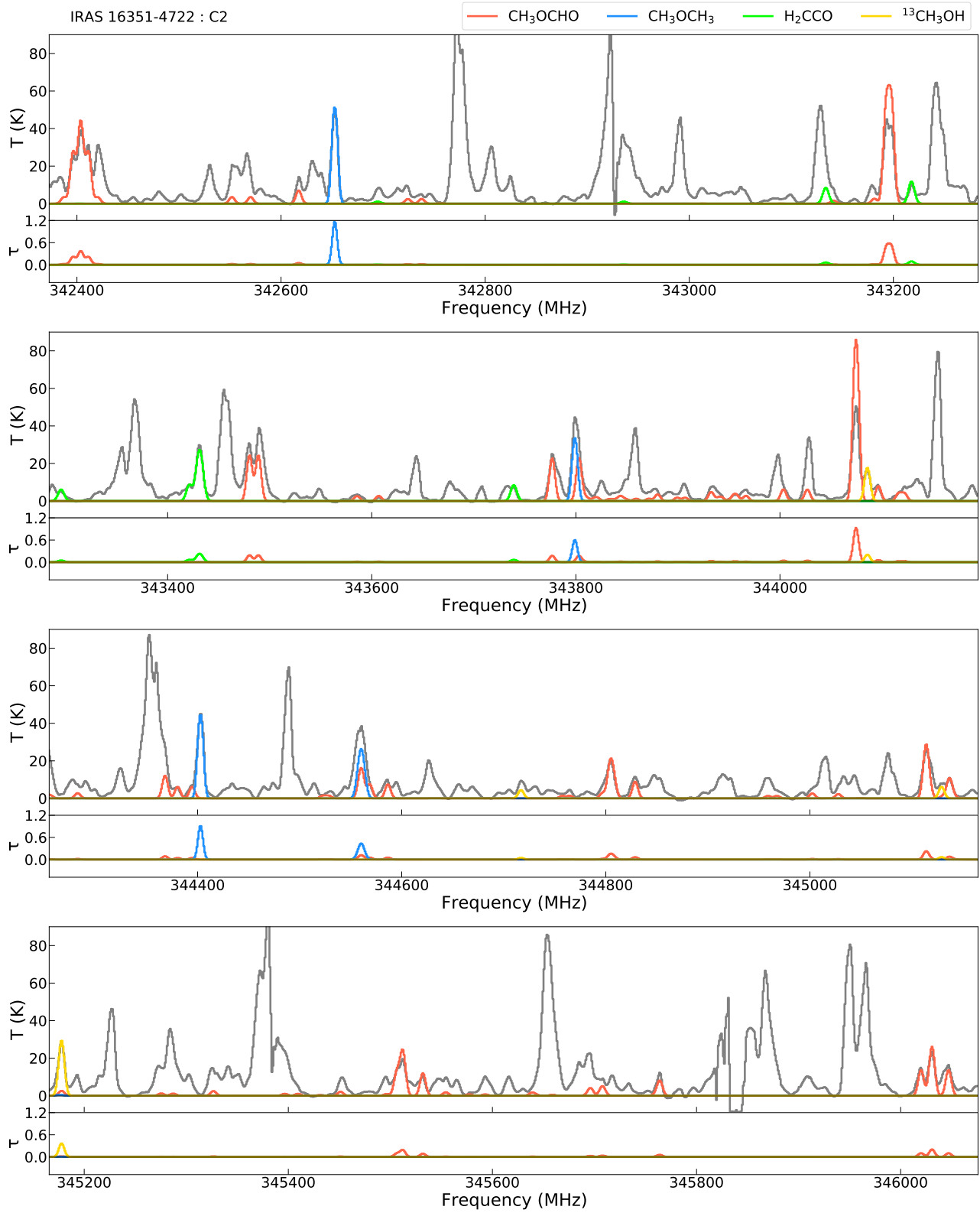


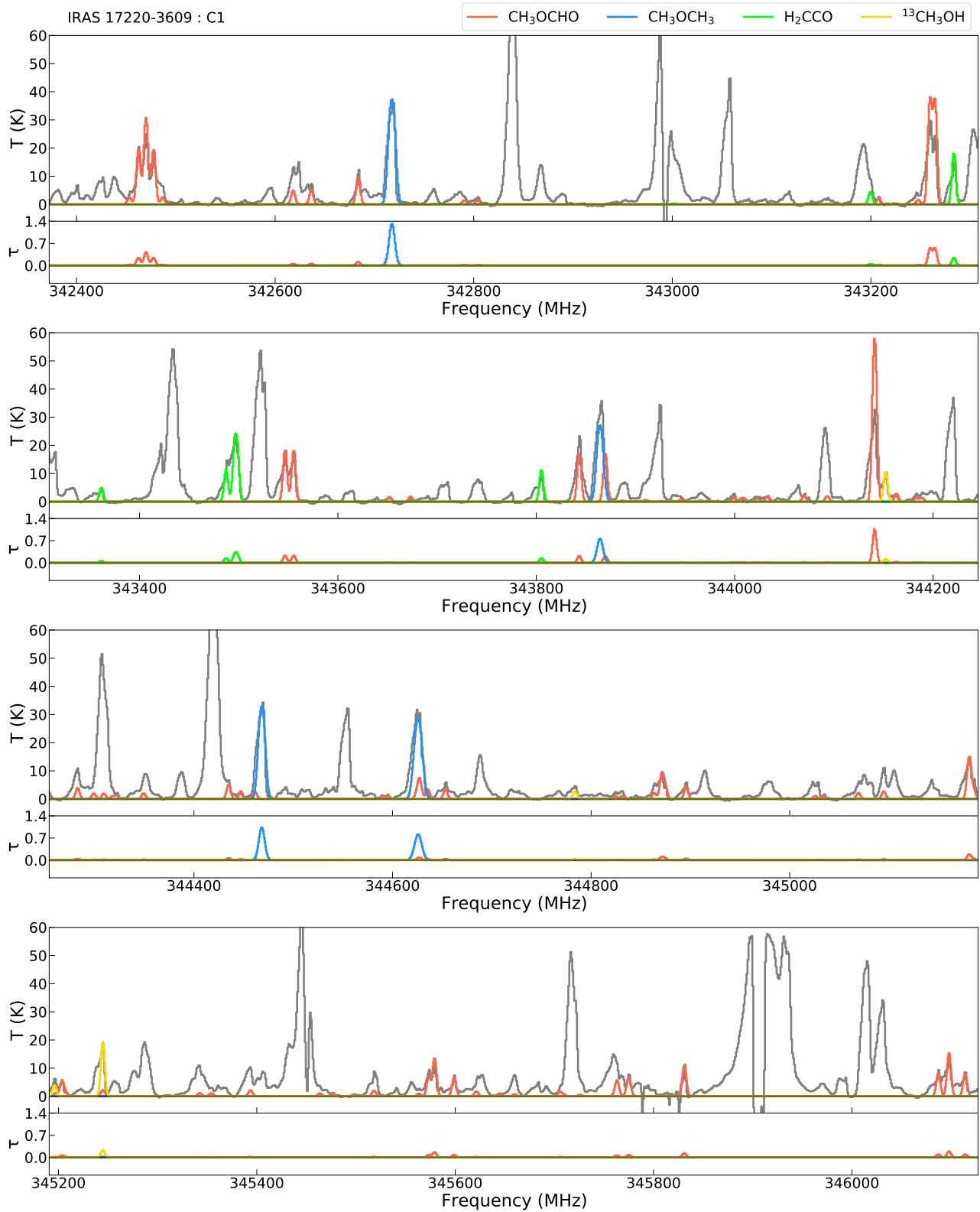






Figure A1. – *continued*





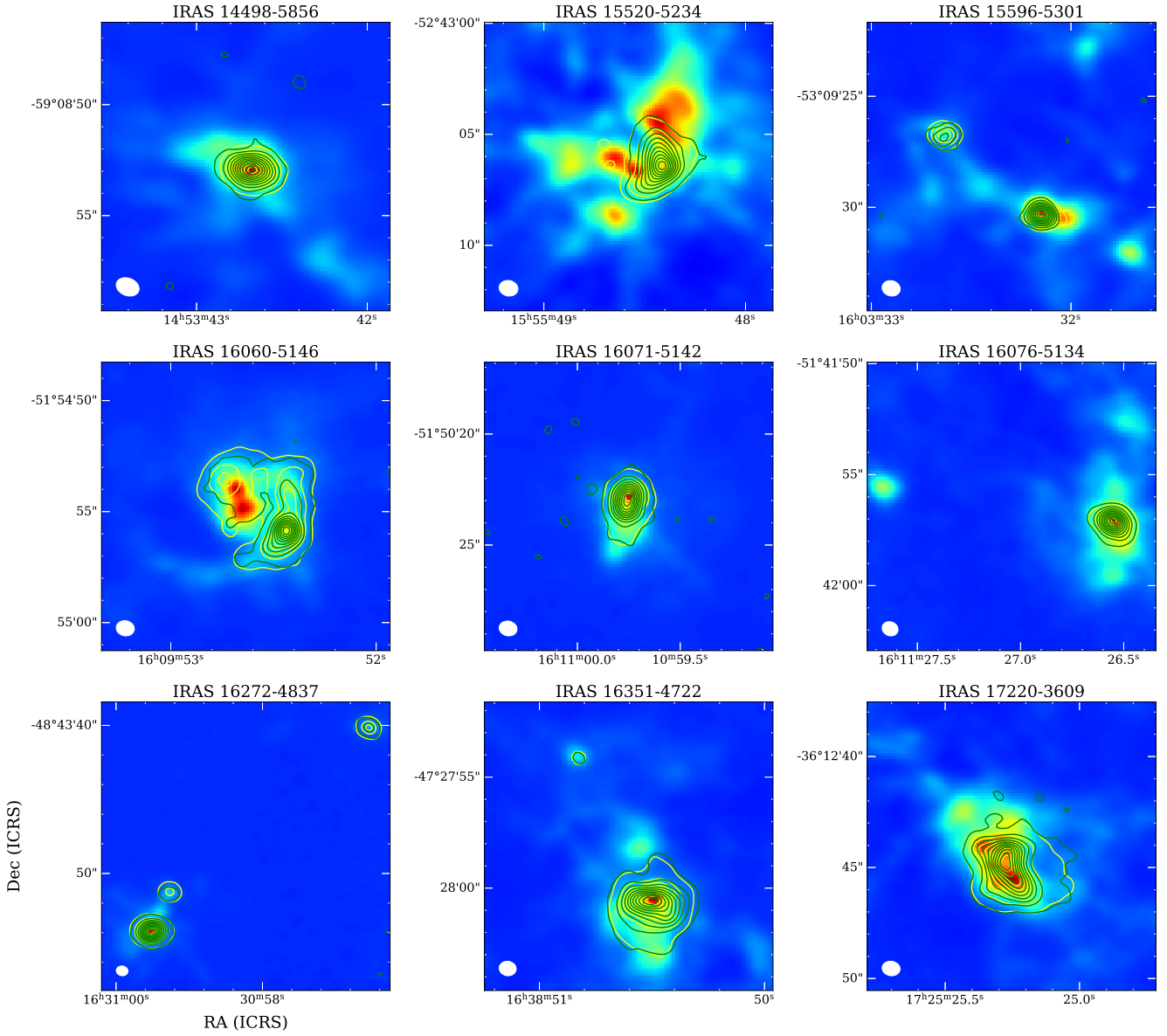


Figure C1. The integrated intensities of CH₃OCHO with different upper energy level transitions. The green and yellow contours represent CH₃OCHO at 342572 MHz ($E_u = 81$ K) and at 342359 MHz ($E_u = 269$ K), respectively. The contour levels are stepped by 10% of the peak values, with the outermost contour levels as follows: I14498: 5%, I15520: 3%, I15596: 8%, I16060: 2%, I16071: 2%, I16076: 6%, I16272: 2%, I16351: 2%, I17220: 2% of the peak values.

Table B1. The Detected Transitions of CH₃OCHO, CH₃OCH₃, and H₂CCO with Signal Above 3 σ Noise Level.

Frequency (MHz)	Transition	S μ^2 (D ²)	E _{up} (K)
CH ₃ OCHO ($\nu=0$)			
342342.185	30(2,28)–29(3,27) E	10.00	269.50
342350.119	30(2,28)–29(3,27) A	10.00	269.49
342351.420	30(3,28)–29(3,27) E	78.04	269.50
342358.225	30(2,28)–29(2,27) E	78.03	269.50
342359.508	30(3,28)–29(3,27) A	78.03	269.49
342366.296	30(2,28)–29(2,27) A	78.03	269.49
342367.680	30(3,28)–29(2,27) E	10.00	269.50
342375.658	30(3,28)–29(2,27) A	10.00	269.49
342506.986	11(8,4)–10(7,4) E	3.46	81.40
342525.299	11(8,3)–10(7,3) E	3.46	81.42
342572.422	11(8,4)–10(7,3) A	3.46	81.41
342572.422	11(8,3)–10(7,4) A	3.46	81.41
342678.725	27(13,15)–27(12,16) E	5.56	335.27
342680.167	27(13,14)–27(12,15) E	5.56	335.28
342692.876	27(13,14)–27(12,15) A	5.56	335.28
342692.888	27(13,15)–27(12,16) A	5.56	335.28
343096.392	17(5,12)–16(4,13) E	1.87	107.82
343136.353	26(13,13)–26(12,14) E	5.23	319.30
343136.356	26(13,14)–26(12,15) E	5.23	319.29
343147.898	31(1,30)–30(2,29) E	11.85	273.44
343148.047	31(2,30)–30(2,29) E	81.50	273.44
343148.169	31(1,30)–30(1,29) E	81.50	273.44
343148.318	31(2,30)–30(1,29) E	11.85	273.44
343149.303	17(5,12)–16(4,13) A	1.87	107.81
343152.958	31(1,30)–30(2,29) A	11.89	273.43
343153.106	31(2,30)–30(2,29) A	81.46	273.43
343153.227	31(1,30)–30(1,29) A	81.46	273.43
343153.376	31(2,30)–30(1,29) A	11.89	273.43
343153.762	26(13,13)–26(12,14) A	5.23	319.30
343153.770	26(13,14)–26(12,15) A	5.23	319.30
343435.260	28(4,24)–27(4,23) E	71.57	257.08
343443.944	28(4,24)–27(4,23) A	71.58	257.08
343539.815	25(13,12)–25(12,13) E	4.90	303.92
343541.355	25(13,13)–25(12,14) E	4.90	303.91
343561.850	25(13,12)–25(12,13) A	4.90	303.92
343561.883	25(13,13)–25(12,14) A	4.90	303.92
343731.783	27(7,20)–26(7,19) E	67.17	258.47
343758.010	27(7,20)–26(7,19) A	67.19	258.48
343798.647	28(23,5)–27(23,4) A	24.44	589.86
343798.647	28(23,6)–27(23,5) A	24.44	589.86
343814.031	28(23,5)–27(23,4) E	24.44	589.86
343826.593	28(23,6)–27(23,5) E	24.44	589.85
343835.114	28(22,7)–27(22,6) A	28.73	560.10
343835.114	28(22,6)–27(22,5) A	28.73	560.10
343854.153	28(22,6)–27(22,5) E	28.74	560.10
343862.096	28(22,7)–27(22,6) E	28.73	560.09
343887.467	28(21,8)–27(21,7) A	32.84	531.66
343887.483	28(21,7)–27(21,6) A	32.84	531.66
343895.152	24(13,11)–24(12,12) E	4.57	289.13
343898.142	24(13,12)–24(12,13) E	4.57	289.13
343909.244	28(21,7)–27(21,6) E	32.83	531.65
343912.685	28(21,8)–27(21,7) E	32.84	531.65
343921.695	24(13,11)–24(12,12) A	4.57	289.14
343921.695	24(13,12)–24(12,13) A	4.57	289.14
343958.362	28(20,9)–27(20,8) A	36.75	504.53
343958.362	28(20,8)–27(20,7) A	36.75	504.53
343981.148	28(20,9)–27(20,8) E	36.74	504.52
343982.450	28(20,8)–27(20,7) E	36.74	504.52
344029.259	32(0,32)–31(1,31) E	10.53	276.10
344029.260	32(1,32)–31(1,31) E	88.18	276.10

Table B1. – *continued*

Frequency (MHz)	Transition	S μ^2 (D ²)	E _{up} (K)
CH ₃ OCHO ($\nu=0$)			
344029.261	32(0,32)–31(0,31) E	88.18	276.10
344029.262	32(1,32)–31(0,31) E	10.53	276.10
344029.645	32(0,32)–31(1,31) A	13.73	276.08
344029.645	32(1,32)–31(1,31) A	84.98	276.08
344029.646	32(0,32)–31(0,31) A	84.98	276.08
344029.647	32(1,32)–31(0,31) A	13.73	276.08
344051.371	28(19,10)–27(19,9) A	40.46	478.72
344051.371	28(19,9)–27(19,8) A	40.46	478.72
344071.196	28(19,9)–27(19,8) E	40.45	478.72
344076.934	28(19,10)–27(19,9) E	40.45	478.72
344170.930	28(18,10)–27(18,9) A	43.97	454.24
344170.930	28(18,11)–27(18,10) A	43.97	454.24
344187.246	28(18,10)–27(18,9) E	43.98	454.24
344197.339	28(18,11)–27(18,10) E	43.97	454.24
344206.436	23(13,10)–23(12,11) E	4.23	274.95
344210.812	23(13,11)–23(12,12) E	4.23	274.94
344237.391	23(13,10)–23(12,11) A	4.23	274.95
344237.414	23(13,11)–23(12,12) A	4.23	274.95
344322.992	28(17,12)–27(17,11) A	47.30	431.09
344322.992	28(17,11)–27(17,10) A	47.30	431.09
344335.357	28(17,11)–27(17,10) E	47.30	431.08
344349.515	28(17,12)–27(17,11) E	47.30	431.08
344477.576	22(13,9)–22(12,10) E	3.89	261.36
344483.461	22(13,10)–22(12,11) E	3.89	261.35
344512.739	22(13,9)–22(12,10) A	3.89	261.37
344512.747	22(13,10)–22(12,11) A	3.89	261.37
344515.454	28(16,13)–27(16,12) A	50.43	409.27
344515.454	28(16,12)–27(16,11) A	50.43	409.27
344523.525	28(16,12)–27(16,11) E	50.43	409.26
344541.314	28(16,13)–27(16,12) E	50.43	409.26
344712.139	21(13,8)–21(12,9) E	3.55	248.37
344719.465	21(13,9)–21(12,10) E	3.55	248.36
344751.514	21(13,9)–21(12,10) A	3.55	248.37
344751.524	21(13,8)–21(12,9) A	3.55	248.37
344759.096	28(15,14)–27(15,13) A	53.37	388.78
344759.096	28(15,13)–27(15,12) A	53.37	388.78
344762.590	28(15,13)–27(15,12) E	53.37	388.78
344783.597	28(15,14)–27(15,13) E	53.38	388.78
344913.684	20(13,7)–20(12,8) E	3.20	235.98
344922.458	20(13,8)–20(12,9) E	3.20	235.97
344957.101	20(13,8)–20(12,9) A	3.20	235.98
344957.127	20(13,7)–20(12,8) A	3.20	235.98
344982.605	47(6,41)–47(5,42) E	2.31	104.43
345067.795	28(14,14)–27(14,13) E	56.12	369.64
345069.059	28(14,15)–27(14,14) A	56.12	369.64
345069.059	28(14,14)–27(14,13) A	56.12	369.64
345073.057	16(6,11)–15(5,10) A	2.71	104.42
345085.394	19(13,6)–19(12,7) E	2.85	224.18
345091.465	28(14,15)–27(14,14) E	56.12	369.64
345095.559	19(13,7)–19(12,8) E	2.85	224.17
345132.629	19(13,6)–19(12,7) A	2.85	224.18
345132.655	19(13,7)–19(12,8) A	2.85	224.18
345230.296	18(13,5)–18(12,6) E	2.48	212.97
345241.935	18(13,6)–18(12,7) E	2.48	212.96
345281.320	18(13,6)–18(12,7) A	2.48	212.97
345281.320	18(13,5)–18(12,6) A	2.48	212.97
345351.333	17(13,4)–17(12,5) E	2.11	202.36
345364.235	17(13,5)–17(12,6) E	2.11	202.34
345385.268	16(6,10)–15(5,10) E	0.40	104.45
345405.869	17(13,5)–17(12,6) A	2.11	202.36

Table B1. – continued

Frequency (MHz)	Transition	$S\mu^2$ (D ²)	E_{up} (K)
CH ₃ OCHO ($v=0$)			
345405.869	17(13,4)–17(12,5) A	2.11	202.36
345451.103	16(13,3)–16(12,4) E	1.73	192.34
345461.011	28(13,15)–27(13,14) E	58.68	351.85
345465.345	16(13,4)–16(12,5) E	1.73	192.32
345466.962	28(13,16)–27(13,15) A	58.67	351.86
345466.962	28(13,15)–27(13,14) A	58.67	351.86
345486.602	28(13,16)–27(13,15) E	58.68	351.85
345509.021	16(13,4)–16(12,5) A	1.73	192.34
345509.021	16(13,3)–16(12,4) A	1.73	192.34
345532.134	15(13,2)–15(12,3) E	1.33	182.91
345547.616	15(13,3)–15(12,4) E	1.33	182.89
345593.318	15(13,3)–15(12,4) A	1.33	182.91
345593.318	15(13,2)–15(12,3) A	1.33	182.91
345596.828	14(13,1)–14(12,2) E	0.91	174.07
345613.535	14(13,2)–14(12,3) E	0.91	174.06
345647.338	13(13,0)–13(12,1) E	0.47	165.83
345650.835	9(9,1)–8(8,1) E	3.90	80.31
345661.070	14(13,1)–14(12,2) A	0.91	174.07
345661.070	14(13,2)–14(12,3) A	0.91	174.07
345662.771	9(9,0)–8(8,0) E	3.90	80.33
345665.188	13(13,1)–13(12,2) E	0.47	165.81
345714.339	13(13,0)–13(12,1) A	0.47	165.83
345714.339	13(13,1)–13(12,2) A	0.47	165.83
345718.662	9(9,1)–8(8,0) A	3.90	80.32
345718.662	9(9,0)–8(8,1) A	3.90	80.32
345974.664	28(12,16)–27(12,15) E	61.04	335.43
345985.381	28(12,17)–27(12,16) A	61.05	335.43
345985.381	28(12,16)–27(12,15) A	61.05	335.43
346001.616	28(12,17)–27(12,16) E	61.04	335.43
CH ₃ OCH ₃ ($v=0$)			
342607.898	19(0,19)–18(1,18) EA	110.05	167.14
342607.898	19(0,19)–18(1,18) AE	165.08	167.14
342607.971	19(0,19)–18(1,18) EE	440.24	167.14
342608.044	19(0,19)–18(1,18) AA	275.16	167.14
343753.320	17(2,16)–16(1,15) EA	29.01	143.70
343753.320	17(2,16)–16(1,15) AE	58.02	143.70
343754.216	17(2,16)–16(1,15) EE	232.07	143.70
343755.112	17(2,16)–16(1,15) AA	87.02	143.70
344357.816	19(1,19)–18(0,18) EA	55.06	167.18
344357.816	19(1,19)–18(0,18) AE	110.12	167.18
344357.929	19(1,19)–18(0,18) EE	440.51	167.18
344358.041	19(1,19)–18(0,18) AA	165.18	167.18
344512.176	11(3,9)–10(2,8) EA	25.13	72.78
344512.219	11(3,9)–10(2,8) AE	12.57	72.78
344515.385	11(3,9)–10(2,8) EE	100.53	72.78
344518.572	11(3,9)–10(2,8) AA	37.70	72.78
H ₂ CCO ($v=0$)			
343088.615	17(5,13)–16(5,12)	93.93	473.85
343088.615	17(5,12)–16(5,11)	93.93	473.85
343172.572	17(0,17)–16(0,16)	34.28	148.30
343250.411	17(4,14)–16(4,13)	32.38	356.84
343250.411	17(4,13)–16(4,12)	32.38	356.84
343376.133	17(2,16)–16(2,15)	33.81	200.53
343384.676	17(3,15)–16(3,14)	99.64	265.71
343387.579	17(3,14)–16(3,13)	99.64	265.71
343693.935	17(2,15)–16(2,14)	33.81	200.61

Notes. The rest frequencies are listed and the transitions are in the form of $J(K_a, K_c) - J'(K_a', K_c')$. The $S\mu^2$ is the product of the line strength and the square of the relevant dipole moment. The E_{up} is the upper level energy of each transition.